Check for updates

Advanced Materials

ADVANCED MATERIALS
www.advmat.de

RESEARCH ARTICLE

Pollen-Engraved Dual Porosity Ceramic Beads From Liquid Marbles for Environmental Remediation

Chenchen Zhou[1,2,3] | Jun Hao Mo[2,3] | Ruiyan Ni[4] | Zihao Guo[5] | Yanzhang Xu[2,3] | Xinyue Zhang[1,2] | Hanna Kim[2,3] | Jian Li[2,3] | Ibrahim Shahrudin Mohammed[2,3] | Munho Kim[5] | Bernard P. Binks[6] | Nam-Joon Cho[2,3]

[1]State Key Laboratory of Micro-Nano Engineering Science, School of Mechanical Engineering, Shanghai Jiao Tong University, Shanghai, China | [2]School of Materials Science and Engineering, Nanyang Technological University, Singapore, Singapore | [3]Centre for Cross Economy, Nanyang Technological University, Singapore, Singapore | [4]College of Textiles, Donghua University, Shanghai, China | [5]School of Electrical and Electronic Engineering, Nanyang Technological University, Singapore, Singapore | [6]Department of Chemistry, University of Hull, Hull, UK

Correspondence: Chenchen Zhou (chenchen.zhou@sjtu.edu.cn) | Nam-Joon Cho (njcho@ntu.edu.sg)

Received: 13 March 2026 | **Revised:** 28 September 2026 | **Accepted:** 12 October 2026

Keywords: dual-porosity ceramics | environmental remediation | liquid marbles | pollen biowastes | wetting transitions

ABSTRACT

Liquid marbles, renowned for their non-wetting behavior, have been extensively investigated in the fields of controlled delivery, droplet reactors, and biomaterial storage. However, the transition in wetting interactions between the liquid droplet and the coating particles has not been clearly studied, and leveraging this transformation for new applications remains unexplored. Here, we use UV irradiation along with mechanical vibration to switch the wetting state at the liquid marble interface from Cassie–Baxter to Cassie-impregnating during a one-step process that converts liquid marbles into ceramic green bodies. Renewable biowaste pollen is, for the first time, employed to impart both surface patterning and internal porosity together with a photocured polymer, yielding dual-porosity ceramic adsorbents that achieve up to 2.88 times higher pollutant removal efficiency, particularly for heavy metal ions and nanoplastics. Furthermore, different pollen species exhibit distinct pollutant selectivity, underscoring their potential for environmental remediation.

1 | Introduction

A liquid marble (LM) is a non-wetting droplet fabricated by depositing and rolling an individual water droplet on a layer of hydrophobic powder such as lycopodium, poly(tetrafluoroethylene), hydrophobized silica, polyethylene, graphite, and carbon black [1–4]. First introduced by Aussillous and Quéré, it was envisioned as a safe method to transport liquids without leakage [5] owing to the proper encapsulation that inhibits coalescence between LMs and ensures safe storage [6]. Their unique characteristics, including low wettability, remarkable separability, easy size/shape tunability, and controlled gas permeability [7–9] make them sought after in many applications, from controlled delivery [10, 11] to precise miniature reactors [12–14] to cell cryopreservation and culture [2, 15, 16].

LM formation relies on the interaction between liquid droplets and solid particles, with low wettability being favored facilitating particles to adhere to the liquid surface rather than dispersing within it. This behavior arises from the replacement of the liquid–vapor interface with the liquid–solid interface reducing the overall surface free energy [4, 7, 17, 18]. Liquid-particle wettability depends on the liquid surface tension and the particle surface energy, with low wettability primarily being a result of high liquid surface tension and low particle surface energy [19, 20]. Furthermore, roughening of the liquid–solid interface reduces

Chenchen Zhou and Jun Hao Mo contributed equally to this work.

All rights reserved, including rights for text and data mining and training of artificial intelligence technologies or similar technologies.
© 2026 Wiley-VCH GmbH

the wettability, trapping air pockets between protrusions of the particles, increasing the contact angle, leading to a Cassie–Baxter (CB) state [21–24]. Contrarily, low liquid surface tension coupled with high surface energy particles results in the transition from the CB to the Wenzel state, increasing wettability and spreading on the surface and inhibiting LM formation [21, 25, 26]. The Cassie-impregnating (CI) state is an intermediate wetting state between the CB and Wenzel states: the droplet remains supported by the tops of surface protrusions but partially enters the texture. As a result, some of the air pockets between protrusions are replaced by liquid [27, 28]. The CI state demonstrates a pronounced liquid–solid interface, underscoring its potential utility in adsorption-related fields, as the increased surface area can improve adsorption performance.

The transition of wetting state can be achieved when sufficient energy is introduced into the system or by modifying the particle surface [29, 30]. Such stimuli include mechanical vibration [29], temperature [31], or UV irradiation [32]. Fujii et al. report that the transition of poly(*N*-isopropylacrylamide) particles from hydrophobic to hydrophilic occurs once the temperature is cooled below its lower critical solution temperature forming thermo-responsive LMs [31]. According to Bormashenko et al., mechanical vibration triggers the transition of wetting state from CB to CI due to sufficient energy input promoting the penetration of liquid into the surface pores [29]. Additionally, Tan et al. demonstrate that UV irradiation can induce surface modification on pollen microparticles transforming their surface from hydrophobic to hydrophilic [32].

Owing to the sporopollenin-rich exine layer, hydrophobic pollen microparticles are widely employed as separating particles for LM formation [3, 33, 34]. Within the same species, pollen exhibits great monodispersity, whereas different pollen species can be distinguished by their unique morphological features [35]. As an organic material, pollen decomposes at a temperature <600°C [36], holding great potential to be introduced as a porogen to control the pore morphologies for porous ceramic adsorbents. The spiky morphology of sunflower pollen grains has been leveraged to imprint nanoscale asperities onto polydimethylsiloxane (PDMS), yielding a superhydrophobic composite [37] which is expected to function as an efficient substrate for LM formation.

In contrast to previous pollen-based LMs, in which the LM serves only as a transient non-wetting container and liquid impregnation into the particle layer is regarded as a failure mode, this study deliberately exploits the wetting transition as a fabrication tool and converts the LM itself into a solid functional material. Pollen is used in three key roles: as hydrophobic separating particles for LMs, as building blocks for a superhydrophobic pollen coating and as porogens for porous ceramic adsorbents. Besides modulating the wetting states from CB toward CI to enhance liquid impregnation into the pollen microstructure and increase liquid–solid interfacial contact, the combination of mechanical vibration [29] and UV irradiation [32] is employed not only to engineer the LM geometry and production but also to facilitate the photocuring of LMs into ceramic green bodies [38, 39]. Simultaneous thermal decomposition of the pollen template and the photocured polymer matrix generates a hierarchically porous network, producing pollen-engraved, dual porosity ceramic beads (PDCBs) specifically engineered for environmental remediation. PDCBs templated with various pollen porogens (lycopodium, sunflower, camellia, olive, and pine) are evaluated against common pollutants including dyes, heavy metal ions, and nanoplastics to establish correlations between the unique pollen-engraved pores and pollutant selectivity. The PDCBs synthesized from LMs retain the intrinsic advantages of porous ceramics—low density, high mechanical strength, superior thermal, and chemical stability [40, 41]—while pollen particle templating markedly increases their specific surface area establishing a sustainable platform for a wide array of environmental-remediation technologies. Furthermore, upcycling pollen—an abundant, renewable biowaste [35]—into high value products exemplifies the resource-efficiency strategies promoted by cross-economy frameworks [42, 43].

2 | Results and Discussion

2.1 | Liquid Marble Automatic Formation Based on Pollen Systems

The aqueous precursor of LMs contains silica nanoparticles (SNPs) as the matrix material to develop the bulk ceramic adsorbent. Various pollen particles (including lycopodium, sunflower, camellia, olive, and pine pollen) are added at 0–5 wt.% into the precursor as porogens. Prepolymer poly(ethylene glycol)diacrylate (PEGDA) and photoinitiator (PI, Darocur 1173) are included to construct the crosslinked network that binds the SNPs and pollen together under UV light. The precursor is well mixed then pumped and injected through a Teflon nozzle which is fixed within a metal sheath to ensure the vertical extrusion direction allowing droplets to continuously drip down (Figure 1a–i and Figure S1). Teflon is chosen as the nozzle material over glass and metal due to its superior hydrophobic properties, which prevent dripping droplets from climbing and adhering to the outer surface of the nozzle (Figure S2). This characteristic enables the stable and uniform fabrication of droplets resulting in better size control. A collection dish with a specially designed pollen-based bottom is positioned at the center of an orbital shaker where it serves to collect and shape the droplets.

To ensure stable fabrication and uniform curing of spherical LMs, the precursor droplets are collected on a specially designed pollen-based platform mounted on a shaker (Figure 1a-iii and Figure S1). The pollen-based platform is comprised of three layers arranged from top to bottom: loosely packed lycopodium pollen bed (LPB), superhydrophobic sunflower pollen-PDMS coating (SPC) and plastic/glass substrate. The hydrophobicity of both LPB and SPC systems is essential for LM formation. Lycopodium pollen (30.8 μm) is characterized by a distinctive honeycomb structure with an average pore size of 4.5 μm (Figure 4i-i and Figure S3a). The exine of lycopodium pollen is composed primarily of sporopollenin, a mechanically robust and chemically inert biopolymer that contains long hydrocarbon chains [44, 45] (Figure S3b,c) rendering it water-repellent.

The structure of lycopodium pollen follows the CB wetting model, where the liquid sits on the ridges of the reticulate surface with air pockets trapped beneath (Figure 1a-ii,iv) [3, 46, 47]. The air–water contact angles for the precursors with different SNP content (21.6, 28.8, and 36.0 wt.%) on LPB are measured as

15214095, 0, Downloaded from https://advanced.onlinelibrary.wiley.com/doi/10.1002/adma.75433 by Nam-Joon Cho - Shanghai Jiaotong University , Wiley Online Library on [21/10/2026]. See the Terms and Conditions (https://onlinelibrary.wiley.com/terms-and-conditions) on Wiley Online Library for rules of use; OA articles are governed by the applicable Creative Commons License

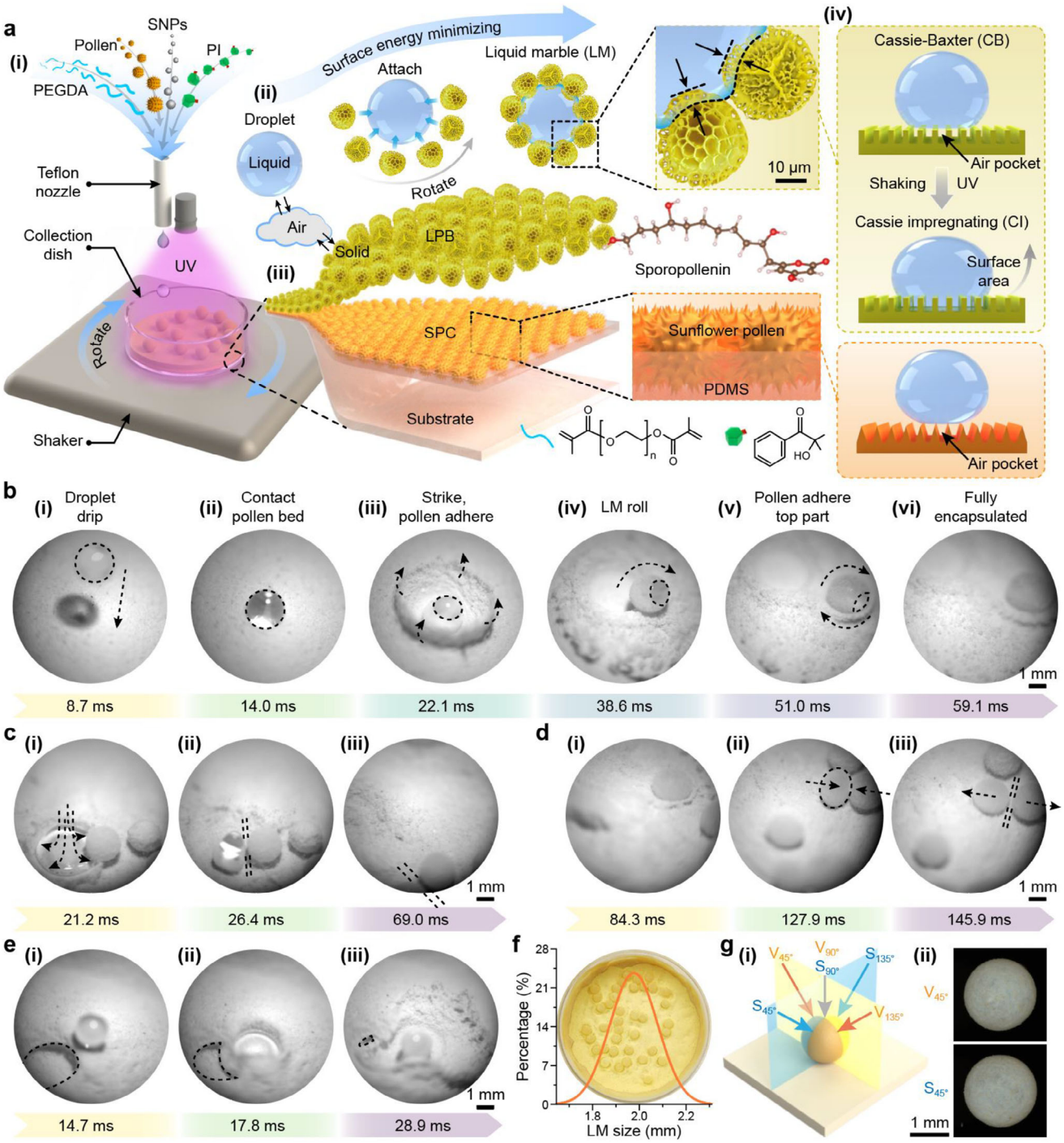


FIGURE 1 | Liquid marble (LM) automatic formation and solidification. (a) Schematic illustration of LM formation. (i) Preparation and extrusion of the precursor containing poly(ethylene glycol) diacrylate (PEGDA), SNPs, photoinitiator (PI), and pollen porogens (0–5 wt.%) through a Teflon nozzle under UV irradiation. (ii) Formation of a precursor droplet governed by the liquid–air–solid interfacial configuration. (iii) Pollen attachment and LM rolling on the collection dish consisting of a lycopodium pollen bed (LPB), a superhydrophobic sunflower pollen–polydimethylsiloxane (PDMS) coating (SPC), and a supporting substrate. (iv) Wetting transition from the CB to CI state. (b) High-speed camera frames illustrating a single LM formation: (i) droplet dripping, (ii) contact with pollen bed, (iii) pollen attachment, (iv) LM rolling, (v) upper-surface encapsulation, and (vi) fully encapsulated LM. (c) Collision between a dripping LM and a rolling LM without coalescence: (i) approach, (ii) contact, and (iii) separation. (d) Rebound between two rolling LMs: (i) approach, (ii) collision, and (iii) separation. (e) Droplet deformation on the pollen bed: (i) initial contact, (ii) flattening, and (iii) recovery. (f) Photograph and size distribution curve showing the homogeneity of the solidified LM green bodies (LMGBs) in the collection dish. (g) Multi-angle stereomicroscopic characterization of a representative LMGB. (i) Schematic illustration of the viewing directions used for imaging. (ii) Representative optical images acquired from $V_{45°}$ and $S_{45°}$, demonstrating the spherical three-dimensional (3D) geometry of the LMGB.

15214095, 0, Downloaded from https://advanced.onlinelibrary.wiley.com/doi/10.1002/adma.75433 by Nam-Joon Cho - Shanghai Jiaotong University , Wiley Online Library on [21/10/2026]. See the Terms and Conditions (https://onlinelibrary.wiley.com/terms-and-conditions) on Wiley Online Library for rules of use; OA articles are governed by the applicable Creative Commons License

134.3°, 135.9°, and 138.1°, respectively (Figure S4). The droplets extruded from the nozzle form spheres under influence of surface tension (Figure 1b-i,ii). After dripping down onto the LPB, the nearest pollen particles self-assemble around the droplet to form an outer packed powder layer (Figure 1b-iii), during which the energy has been rearranged by replacing a spherical cap-shaped portion of the droplet's liquid-air and particle's solid-air interface with a solid–liquid interface across the attachment area to minimize total surface free energy (Figure 1a-ii,b-iii–vi) [17, 48]. Lycopodium powder spreads out forming an inverted dome-shaped pit (Figure 1b-iii). The partially covered droplet rolls and climbs out of the pit under the effect of shaking (Figure 1b–iv). The top part of liquid droplet is then further covered with pollen powder (Figure 1b-v,vi). From contacting to being fully encapsulated, it takes about 45 ms for an LM to be formed (Video S1). The next droplet continues to strike onto LPB and forms a disk-like shape spreading and touching the surrounding LMs (Figure 1c-i). The droplet doesn't coalesce with the LM in contact; instead, it recovers to spherical shape under surface tension and keeps a certain distance from the nearby LM (Figure 1c-ii,iii and Video S2). During the shaking process, LMs roll around on LPB (Figure 1d-i) and hit against each other (Figure 1d-ii). Although they are squeezed into ellipsoids, the LMs remain discrete and bounce back after collision (Figure 1d-iii and Video S3). In addition, the striking and rolling of droplets also assist in filling up the pits and smoothing out the LPB (Figure 1e and Video S4). After shaking and exposure under UV light, the wetting state between liquid droplet and pollen microparticles transforms from CB to CI. To validate these stimulus-induced wetting changes, time-resolved in situ wetting measurements were performed by simultaneously monitoring the contact angle and droplet–pollen surface contact length (Figure S5 and Videos S5–S8). After 10 min of UV pretreatment, the initial contact angle decreased by 6.25%, while the contact length increased by 16.17%, demonstrating enhanced liquid spreading and solid–liquid interfacial contact on the pollen surface. This behavior is attributed to UV-induced modification of the pollen surface chemistry, particularly the increase in oxygen-containing functional groups, which renders the pollen surface more hydrophilic and promotes liquid impregnation [30, 32]. Likewise, mechanical vibration caused the contact length to increase rapidly by 20.73% within the first minute, accompanied by a 5.56% decrease in contact angle. This vibration-enhanced wetting is likely associated with overcoming the energy barrier for liquid penetration and displacing trapped air pockets within the pollen microstructure, thereby facilitating the transition toward the CI state [47].

The LMs are cured by UV exposure and discretely distributed on the LPB with a narrow unimodal size distribution (Figure 1f). Multi-angle stereomicroscopic imaging and continuous rotational observation further confirm the uniform spherical three-dimensional (3D) geometry of the LMGBs (Figure 1g and Figure S6; Video S9). Both LPB and SPC are essential for the stable formation of LMs. Without them, the droplets directly strike the collection dish, stick to the bottom and merge into a freeform pool of liquid forming a chunk after UV solidification (Figure 2a, Control). For the case with only LPB, the droplets strike and pass through the LPB buffer zone hitting the substrate. The pollen particles are expelled from the impact zone of the droplets, resulting in the adherence of the liquid droplets to the substrate (Figure 2a, LPB). The SPC is made by half-embedding the defatted sunflower pollen particles inside the binder PDMS (Figure 2b). The sporopollenin's hydrophobic nature and protruding spikes out of the SPC surface result in a superhydrophobic surface similar to that of lycopodium pollen. The contacting droplets sit on the spikes with air pockets trapped in between cohering with the CB state (Figure 1a(iv)). The air–water contact angles of the precursors with different SNP content on SPC are measured to be 143.1°, 143.2°, and 145.8°, respectively (Figure 2c). For the case with only SPC, LMs can be fabricated with a better ellipsoidal shape. However, the strong impact of the droplet on SPC without the LPB cushion as well as the UV-induced hydrophilization makes the LMs stick to the SPC with the liquid entering the interspace between spikes and wetting the sunflower pollen surface (Figure 2a, SPC), resulting in the incoming liquid droplets coalescing with previous ones. For the case with both SPC and sufficient thickness of LPB, LMs can be fabricated with the desired uniform geometry (Figure 2a, LPB + SPC). LPB thickness (h) has a great impact on LM formation. As h increases, the yield of well-dispersed, spherical, and uniform LMs first increases then decreases with $h = 1$ mm recording the highest yield when the UV source height and shaking speed are set as 30 mm and 250 rpm, respectively (Figure 2d). When h is relatively small, the LPB is incapable of providing sufficient cushion to reduce the droplets' impact on SPC, resulting in the LM splitting with tiny satellite droplets left on SPC (Figure 2e and Video S10) which becomes the culprit for the bottom capture of the subsequent droplets (Figure 2f and Video S11). Afterward, the next droplet strikes onto the captured droplet and coalesces with it due to the contact of the bottom liquid while expelling the redundant pollen particles (Figure 2g and Video S12). However, when h is relatively large, the impacted dent is too deep for the LM to climb out and roll resulting in forming a LM with an unwrapped top and subsequent coalescence of multiple LMs (Figure 2h).

2.2 | Fabrication of LM Green Bodies (LMGBs)

Besides the factor of LPB thickness, the shaking speed (R), nozzle diameter (d) and surface tension (γ) of the precursor also influence the LMGB fabrication in terms of yield, size, sphericity, and so forth. The yield of LMGB's experiences a linear increase as R increases from 0 to 250 rpm and a slight decrease past 250 rpm (Figure 3a). Without sufficient kinetic shaking energy input, the LM is unable to roll on the LPB sufficiently to capture enough pollen particles to encapsulate its bare top (Figure 1b-iii,iv), resulting in the coalescence of the LM after colliding with the following droplets (Figure 2g-i). However, when $R \geq 250$ rpm, LMGBs are measured to have a significantly larger disparity both in their size and sphericity distribution (Figure 3b–d), with 250 rpm recording the narrowest distribution in size of 2.303 mm and out-of-roundness (OR) of 0.0765. Clumpy and irregular LMGBs are formed at higher shaking speeds (Figure 3d–ii,e), because satellite droplets are generated and air is trapped inside LMs under the influence of increased centrifugal force [2, 49]. Moreover, the LMs are hard to cure in this case due to the UV-protection nature of the pollen [50] and enhanced crosslinking inhibition effect from oxygen after LM cleavage [51, 52]. When the shaking speed is fixed at 250 rpm, as d increases the size of LMGB's gradually increases and approaches saturation at 2.4 mm after the nozzle size reaches 0.876 mm (Figure 3f).

15214095, 0, Downloaded from https://advanced.onlinelibrary.wiley.com/doi/10.1002/adma.75433 by Nam-Joon Cho - Shanghai Jiaotong University , Wiley Online Library on [21/10/2026]. See the Terms and Conditions (https://onlinelibrary.wiley.com/terms-and-conditions) on Wiley Online Library for rules of use; OA articles are governed by the applicable Creative Commons License

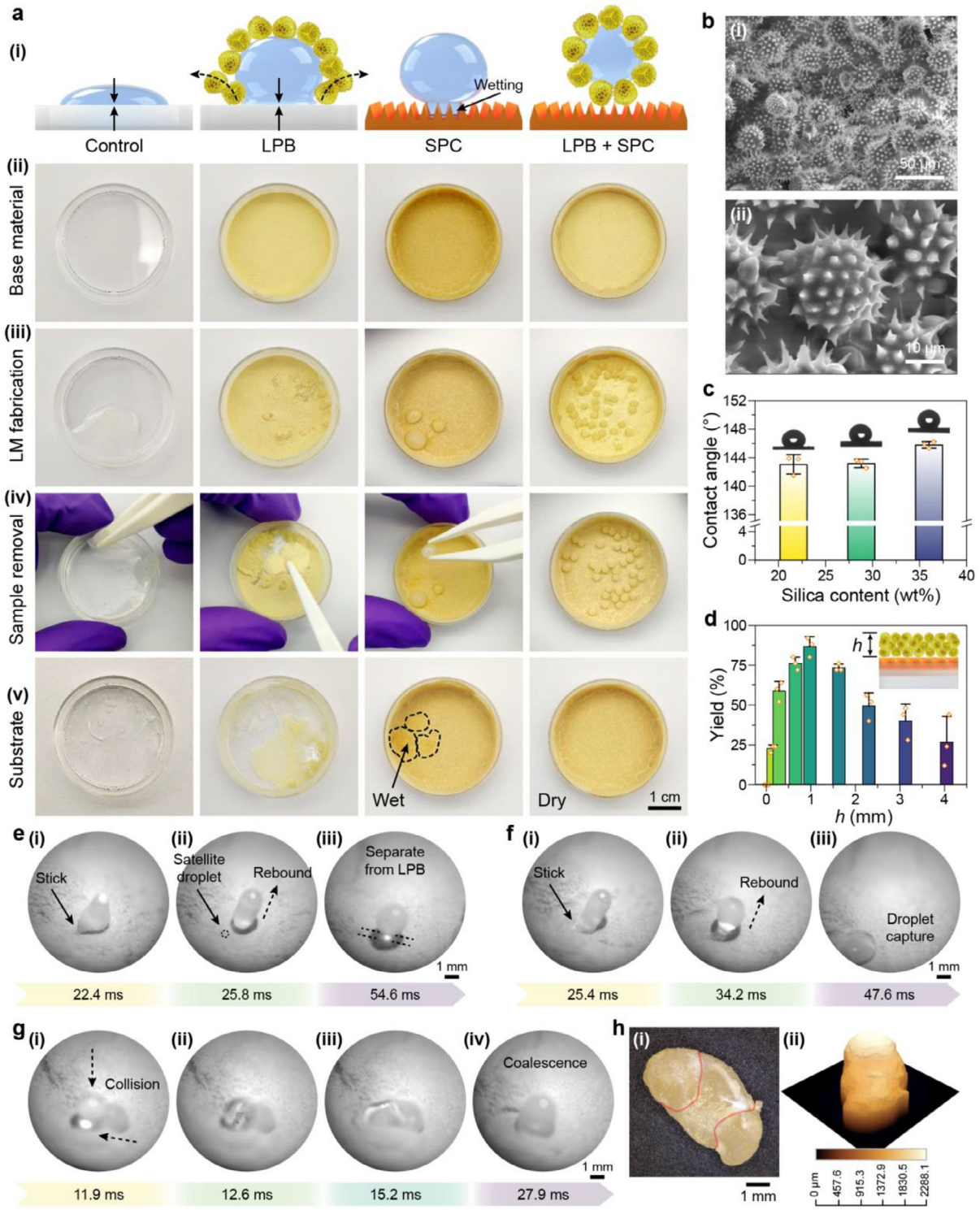


FIGURE 2 | LM formation under different conditions. (a) LM formation in the collection dish under four conditions (columns): without LPB and SPC (Control), with only LPB, with only SPC, and with both LPB and SPC. Rows show (i) the schematic wetting/encapsulation behavior and collection-dish photographs of (ii) the base material before dripping, (iii) after LM dripping and curing, (iv) during sample removal, and (v) the substrate after removal. LMs coalesce under the first three conditions and remain separated and in good shape only with both LPB and SPC. (b) SEM images of the SPC surface at (i) low and (ii) high magnification, showing the half-embedded spiky sunflower pollen. (c) Contact angles of LM precursors with three different silica contents on SPC. (d) Yield of uniform LM versus thickness h of LPB. (e) High-speed camera frames illustrating the coalescence inducer—satellite droplet was split from LM and stuck onto SPC: (i) sticking, (ii) satellite-droplet separation and rebound, and (iii) separation from the LPB. (f) High-speed camera frames showing that the dripping droplet was captured by the SPC through the satellite droplet: (i) sticking, (ii) rebound, and (iii) droplet capture. (g) High-speed camera frames showing the coalescence process of the dripping droplet with the captured droplet: (i) collision, (ii, iii) deformation/contact, and (iv) coalescence. (h) Optical characterization of a coalesced LM formed with a thick LPB (h = 4 mm): (i) top–down optical image and (ii) 3D surface reconstruction.

15214095, 0, Downloaded from https://advanced.onlinelibrary.wiley.com/doi/10.1002/adma.75433 by Nam-Joon Cho - Shanghai Jiaotong University , Wiley Online Library on [21/10/2026]. See the Terms and Conditions (https://onlinelibrary.wiley.com/terms-and-conditions) on Wiley Online Library for rules of use; OA articles are governed by the applicable Creative Commons License

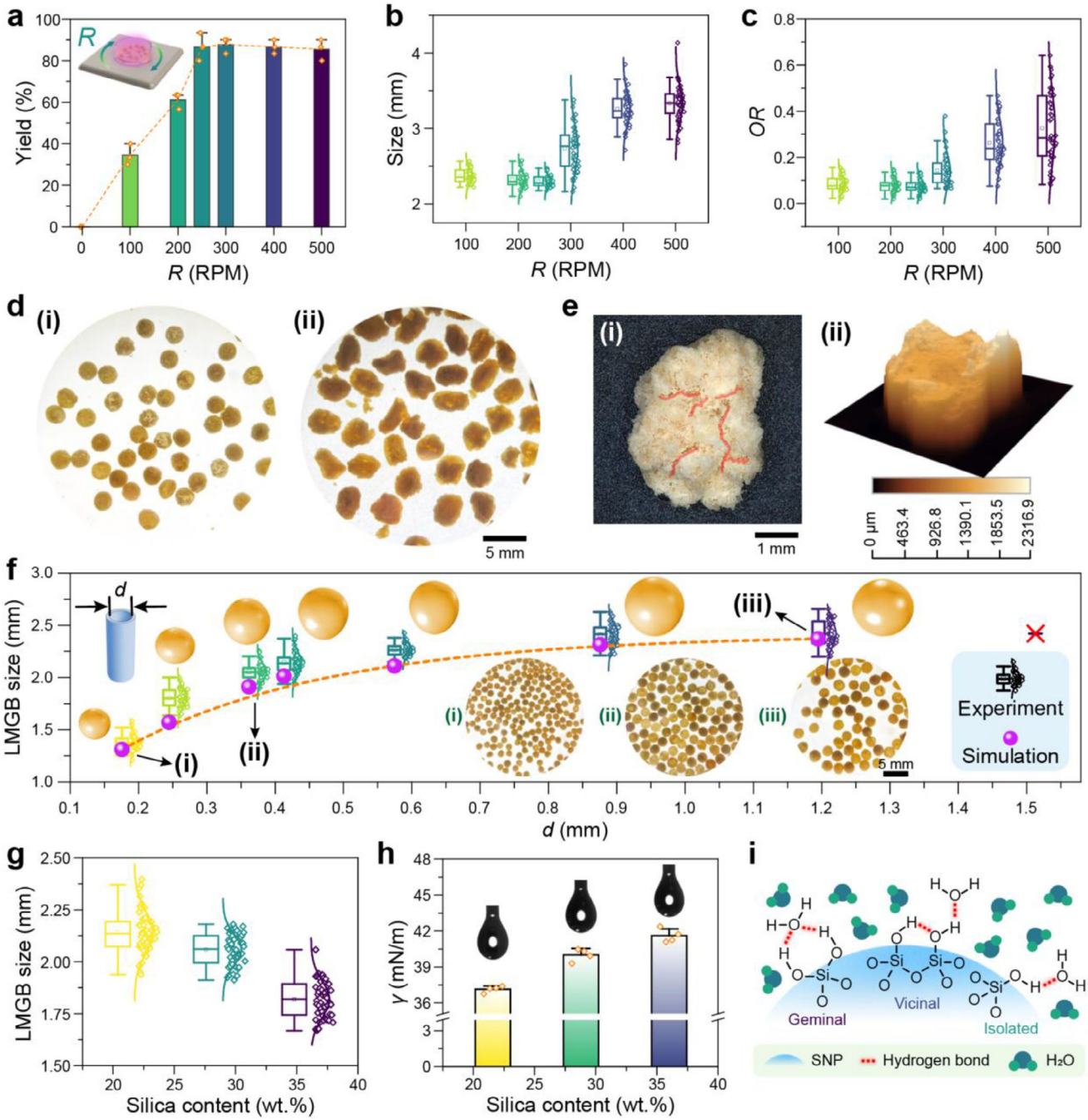


FIGURE 3 | Adjustable fabrication of LM green bodies (LMGBs). (a) Yield as a function of shaking speed (R) showing that it rises and then slightly decreases as R increases. (b) LMGB size versus R showing that the size distribution reaches its narrowest at 250 rpm. (c) Out-of-roundness (OR) versus R showing the most uniform and spherical shape at 250 rpm and significantly increased irregularity above this. (d) Optical microscope images of LMGBs fabricated at (i) 250 and (ii) 500 rpm. (e) Top–down layer-by-layer optical scanning images of an irregular LMGB fabricated at 500 rpm. (f) Size variation of LMGBs with the inner diameter (d) of Teflon nozzle. Experimental and simulation results match and both indicate that the LMGB size increases with d and reaches saturation as $d \approx 0.876$ mm. (g) Size variation of LMGBs with silica content of precursor. (h) Surface tension (γ) of LM precursors versus silica content. (i) Schematic illustration of hydrogen bond formation on the surface of SNPs.

This trend and the saturation behavior are corroborated by computational fluid dynamics simulations of the LM formation process. LMGB formation is recorded to be affected by the contents of components in the precursor as well. Silica content is focused on since it constitutes the majority of the precursor and has a decisive effect on the sintered structure of subsequent PDCBs. Higher silica content leads to the formation of smaller LMGBs (Figure 3g) due to the increased surface tension (Figure 3g,h) [53]. When the SNPs are dispersed in water, their surface consists entirely of silanol groups, including isolated (non-hydrogen bonded), vicinal (hydrogen bonded), and geminal (two silanol groups attached onto the same silicon atom) silanol groups forming hydrogen bonds with surrounding water molecules (Figure 3i) [54–58].

15214095, 0, Downloaded from https://advanced.onlinelibrary.wiley.com/doi/10.1002/adma.75433 by Nam-Joon Cho - Shanghai Jiaotong University , Wiley Online Library on [21/10/2026]. See the Terms and Conditions (https://onlinelibrary.wiley.com/terms-and-conditions) on Wiley Online Library for rules of use; OA articles are governed by the applicable Creative Commons License

2.3 | LMGB Transformation Into PDCBs

LMGBs undergo a two-step heat treatment process, beginning with the removal of organic components followed by the consolidation and densification of the SNPs through sintering (Figure 4a–c). After air drying overnight, the LMGBs show a slight mass loss from room temperature to ~125°C, which is mainly attributed to the evaporation of residual water. Between ~125°C and ~284°C, the polymer inside the LMGBs experience two sequential endothermic processes: glass transition and melting. Over this period, the polymer evolves from a rigid, glassy state to a soft, rubbery state and ultimately to a liquid state [59, 60]. A major weight loss and substantial exothermic heat release subsequently occurs from ~284°C to ~402°C, corresponding to the progressive thermal decomposition of PEGDA and pollen into smaller molecules, water vapor and other volatiles. Upon further heating from ~402°C to ~544°C, the remaining organic residues undergo oxidative combustion in air, resulting in an additional mass loss accompanied by a modest exothermic heat release. Above ~544°C, no significant additional organic-related mass loss is observed, indicating that the organic components have been removed, while subsequent high-temperature treatment promotes consolidation and densification of the silica framework. The magnitude of weight loss and the associated thermal events depend on the relative amounts of silica and pollen in the formulation: a lower silica content and higher pollen content generally result in greater total mass loss (Figure 4a and Table S1). A specimen containing 20.1 wt.% silica and 5 wt.% pollen shows the largest weight loss at 64.7%, whereas a formulation with 36 wt.% silica and 0 wt.% pollen exhibits the smallest loss at 44.1% (Figure 4a). During the debinding process, temperature is ramped slowly at 0.5°C/min to limit abrupt mass- and volume-related stresses that could provoke cracking and ensure the quality of the final sintered product. FTIR analysis further confirms the removal of organic components during thermal treatment (Figure S7). Lycopodium pollen and the corresponding green body exhibit characteristic organic-associated bands, including O–H, aliphatic C–H, C═O, and C–H bending/rocking vibrations, whereas these bands disappear after sintering. In contrast, the spectrum of the sintered PDCB is dominated by the characteristic Si–O–Si stretching bands [61], indicating effective removal of the pollen and polymer components and the formation of a predominantly silica-based ceramic framework.

After sintering, the beads undergo isotropic linear shrinkage while their monodispersity, shape retentivity, and shape fidelity remain well preserved (Figure 4d and Figure S8). The surface of the silica bead is engraved and densely distributed with lycopodium-structured cavities (Figure 4e,f), which verify the CI wetting state of LMs mentioned earlier and the resulting deeper engraving of the pollen microstructure into the bead surface. The silica beads are shown to consist of two elements, silicon and oxygen (Figure 4e), and to possess the crystal structure corresponding with cristobalite (Standard PDF#39-1425, Figure 4f). The porosity increases approximately linearly with increasing pollen content (Figure 4g). The sample prepared without pollen porogens (0 wt.% pollen) is defined as the control and exhibits a porosity of 26.1%, which increases to 56.6% upon the addition of 5 wt.% lycopodium pollen.

Different pollen species, including lycopodium, sunflower, camellia, olive, and pine, are employed as natural porogens to generate distinct pollen-templated pores within the silica beads, enabling tunable pore structures (Figure 4h,i). To directly evaluate the contribution of pollen templating, the pollen-free control is included for comparison in Figure 4h. At a fixed pollen content of 1 wt.%, the porosities of lycopodium-, sunflower-, camellia-, olive-, and pine-templated PDCBs are 31.6%, 47.3%, 39.3%, 31.7%, and 45.1%, respectively, all higher than that of the pollen-free control (26.1%). Micro-CT imaging further reveals the internal pore architecture of the lycopodium-templated PDCBs (Figure S9). Sequential XY-plane slices show pollen-templated cavities distributed throughout the ceramic framework, with channel-like connections between neighboring cavities, confirming the formation of an interconnected open-pore network. A representative cavity extends across approximately 60 slices at a slice interval of 0.3 μm, corresponding to a characteristic dimension of ~18 μm, consistent with the size of the lycopodium pollen-templated pores after sintering. BET measurements further reveal pronounced pollen-species-dependent differences in the accessible surface area of the PDCBs. The pollen-free control exhibits a specific surface area of 0.323 $m^2\ g^{-1}$, whereas the values for lycopodium-, sunflower-, camellia-, olive-, and pine-templated PDCBs are approximately 1.141, 0.491, 0.481, 0.347, and 1.169 $m^2\ g^{-1}$, respectively (Figure S10). Notably, the specific surface areas of the lycopodium- and pine-templated PDCBs are approximately 3.53 and 3.62 times that of the pollen-free control, respectively, demonstrating a substantial increase in accessible surface area induced by these pollen templates. Consistently, the N_2 adsorption–desorption isotherms show markedly higher N_2 uptake for the lycopodium-templated PDCBs than for the pollen-free control over the entire relative-pressure range, further confirming the increased accessible surface area after pollen templating. These results demonstrate that the introduction of pollen effectively increases the porosity of the PDCBs, while the distinct size, morphology, and density of different pollen species further modulate the resulting pore architecture and microenvironment. In addition to the pollen-templated pores, interconnected pores with a characteristic size of approximately 0.58 μm are generated within the beads following the removal of the PEGDA polymer.

2.4 | PDCB Application in Pollutant Removal

PDCB is well suited for environmental remediation because it unites high adsorption capacity with practical handling advantages: it is easier to transport, store, deploy, package, and retrieve than conventional powdery adsorbents [62–66]. The PDCBs are packed into a tube (Figure 5a) creating a cartridge that removes pollutants from wastewater. The voids between the PDCBs allow water to flow smoothly through the medium. When PDCBs are submerged in water, surface siloxane (Si−O−Si) groups hydrolyze to form silanol (Si−OH) groups. When the surrounding pH exceeds the isoelectric point (pH ~ 2–3), the silanol group deprotonates to $Si-O^-$ rendering the surface electrostatically negative [67–70]. Combining the porous nature and negatively charged surface, PDCBs are expected to be great adsorbents for various pollutants such as dye molecules, heavy metal ions, and

15214095, 0, Downloaded from https://advanced.onlinelibrary.wiley.com/doi/10.1002/adma.75433 by Nam-Joon Cho - Shanghai Jiaotong University , Wiley Online Library on [21/10/2026]. See the Terms and Conditions (https://onlinelibrary.wiley.com/terms-and-conditions) on Wiley Online Library for rules of use; OA articles are governed by the applicable Creative Commons License

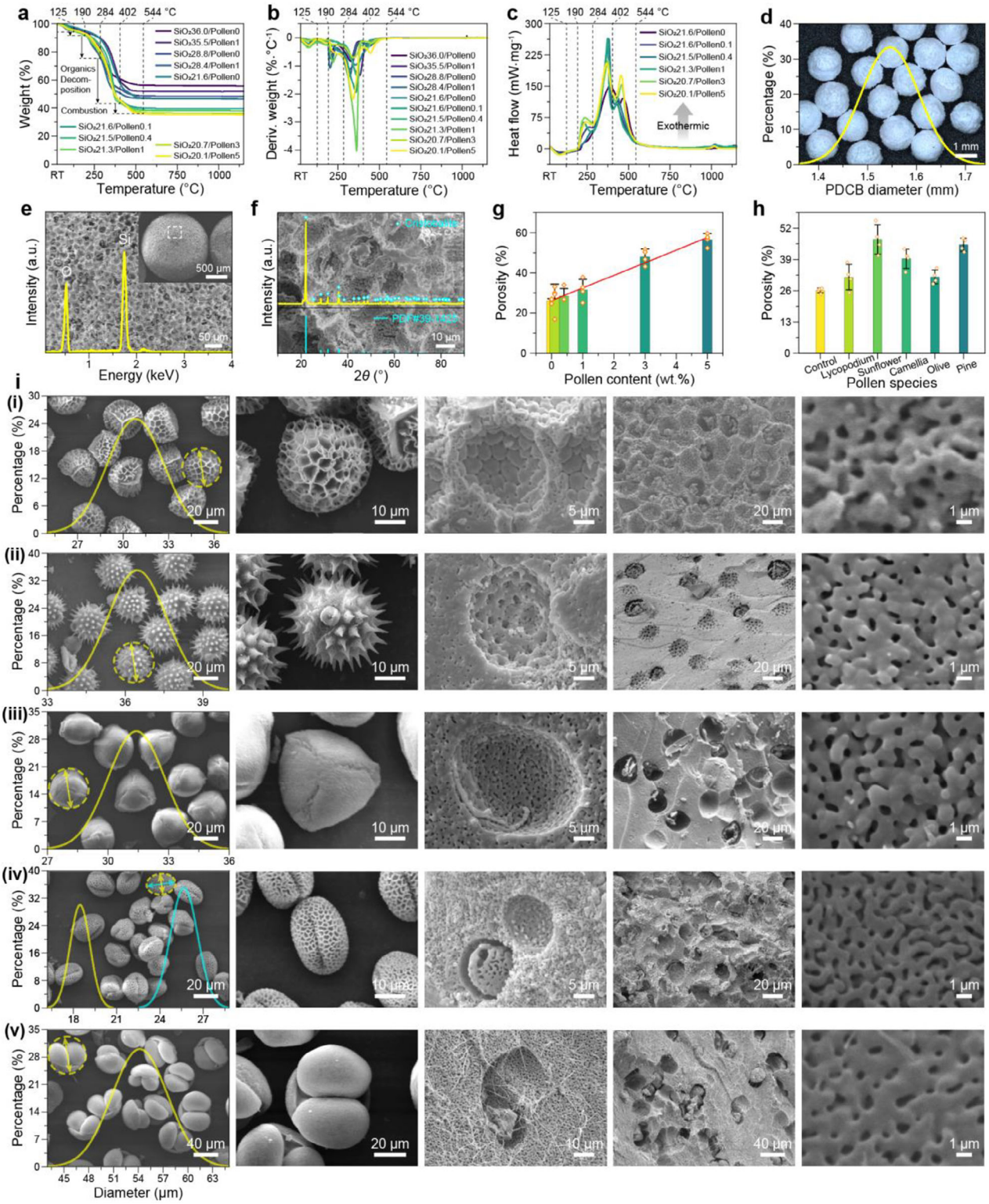


FIGURE 4 | LMGB transformation into pollen-engraved dual PDCBs. (a) Thermogravimetric analysis of LMGB weight change during the sintering process (SiO_2 *x*/pollen *y* represents the sample with *x*% silica and *y*% pollen). (b) Derivative of LMGB weight change with temperature during sintering. (c) Differential scanning calorimetry curves of LMGBs during sintering. (d) Optical image and size distribution curve of sintered PDCBs showing their uniform morphology. (e) SEM image and EDX spectrum of PDCB surface exhibiting the lycopodium pollen-engraved surface pattern and Si and O elemental composition. (f) SEM image of the enlarged surface of PDCB and x-ray diffraction spectrum showing its cristobalite crystalline structure. (g) Variation of PDCB porosity with pollen content, where the pollen-free sample (0 wt.% pollen) serves as the control. (h) Comparison of the porosity of the control and PDCBs templated with different pollen species (1 wt.% pollen). (i) SEM images of various pollen particles including (i) lycopodium, (ii) sunflower, (iii) camellia, (iv) olive, and (v) pine pollen showing their special structures and uniform morphologies and their resultant PDCBs showing the inner pore structures templated by pollen and polymer binder.

15214095, 0, Downloaded from https://advanced.onlinelibrary.wiley.com/doi/10.1002/adma.75433 by Nam-Joon Cho - Shanghai Jiaotong University , Wiley Online Library on [21/10/2026]. See the Terms and Conditions (https://onlinelibrary.wiley.com/terms-and-conditions) on Wiley Online Library for rules of use; OA articles are governed by the applicable Creative Commons License

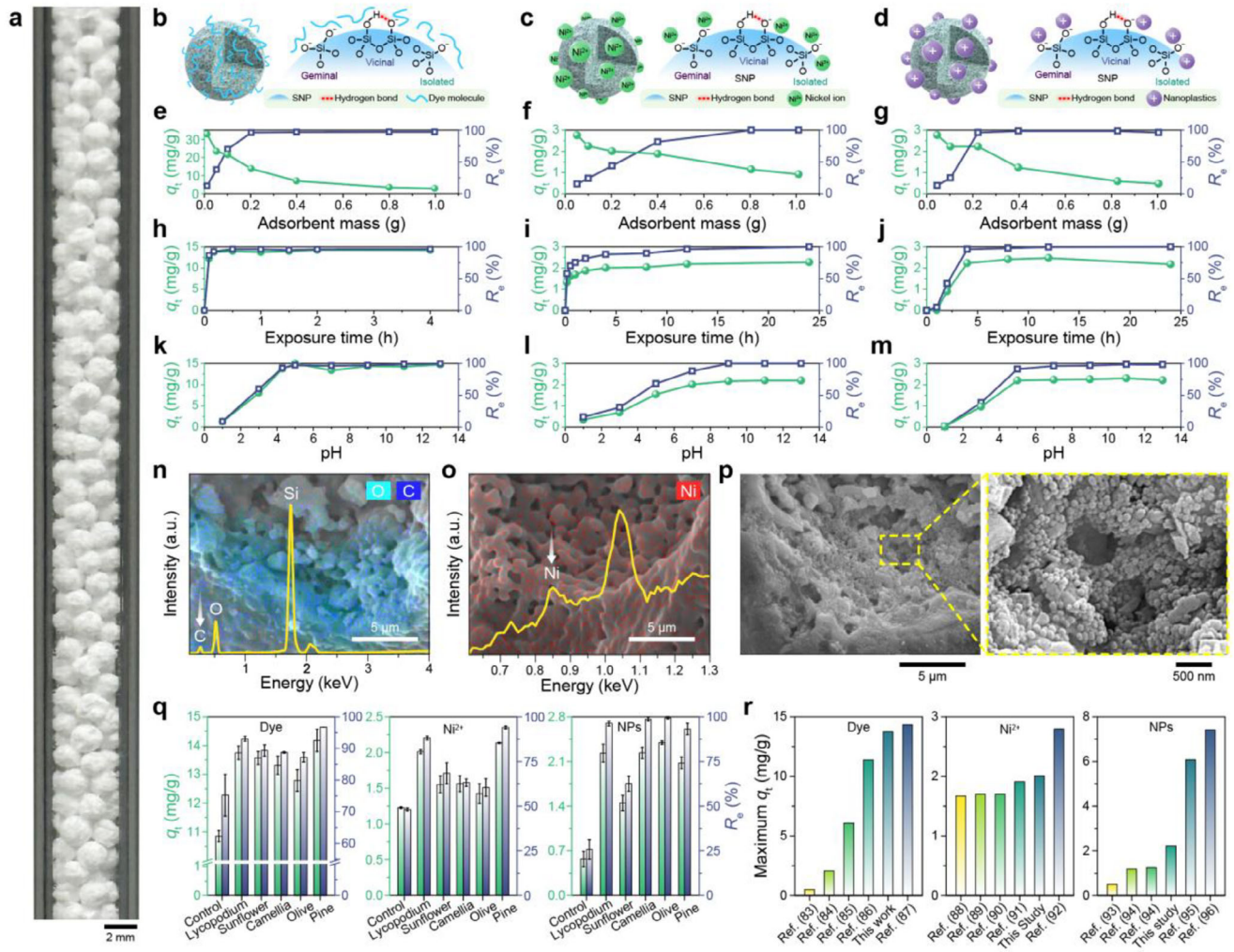


FIGURE 5 | Environmental remediation performance of PDCBs. (a) Photograph of PDCBs packed in a column. Schematic illustration of PDCB adsorption for (b) dye molecules, (c) nickel ions, and (d) nanoplastics (NPs). Effects of adsorbent mass on adsorption capacity (q_t) and removal efficiency (R_e) for (e) dye molecules, (f) nickel ions, and (g) NPs. Effects of contact time on q_t and R_e for (h) dye molecules, (i) nickel ions, and (j) NPs. Effects of solution pH on q_t and R_e for (k) dye molecules, (l) nickel ions, and (m) NPs. EDX elemental mapping and spectrum of PDCB (n) after dye adsorption and (o) nickel ions adsorption. (p) SEM images showing NPs retained within the porous structure of PDCBs. (q) Comparison of q_t and R_e among the pollen-free control and PDCBs templated with different pollen species for dye molecules, nickel ions, and NPs. (r) Comparisons of the maximum adsorption capacities of PDCBs with previously reported adsorbents for dye molecules [83–87], nickel ions [88–92], and NPs [93–96]. All the data in (e–m), (q) are presented as mean ± s.d. from ≥ 3 samples.

nanoplastics (NPs) (Figure 5b–d). In addition, silanol groups present on the pore walls enable organic molecules to form strong hydrogen bonds and exhibit dipole-dipole interactions with the surface of silica, promoting adsorption [71, 72]. The effects of PDCBs and their adsorption properties are explored by investigating the adsorption capacity (q_t) and removal efficiency (R_e) against adsorbent mass, exposure time, and solution pH.

Organic dye molecules were used to evaluate the adsorption performance of PDCBs. At a fixed contact time of 1 h, increasing the PDCB mass from 0.01 to 1.0 g increased the R_e from 12.3% to 97.1%, while decreasing the q_t from 32.74 to 2.81 mg g^{-1} (Figure 5e). The enhanced R_e arises from the greater number of available adsorption sites at higher mass, whereas the decline of q_t reflects a lower amount of dye adsorbed per unit adsorbent mass under a fixed initial dye concentration [73]. Based on the high R_e of 96.3% obtained at 0.2 g, this PDCB mass was selected to investigate the effect of exposure time on adsorption performance (Figure 5h). Dye uptake proceeds rapidly during the initial adsorption stage, reaching a q_t of 12.2 mg g^{-1} and R_e of 86.5% within 5 min. Thereafter, adsorption gradually approaches saturation after 10 min as the readily available active sites become progressively occupied, limiting further dye uptake [74, 75]. The pH-dependent adsorption profile (Figure 5k) suggests that electrostatic attractions participate in the removal of dye molecules. The removal of dye experienced low adsorption rates at pH 1, with a q_t and R_e of 1.28 mg g^{-1} and 8.7%, respectively. Under acidic conditions, the high concentration of hydrogen ions competes with dye for the negatively charged adsorption sites, resulting in the subpar removal of dye molecules. As the pH increased, deprotonation of the silanol groups facilitates the transition toward a more negatively charged PDCB surface, enhancing the electrostatic attraction toward dye molecules.

15214095, 0, Downloaded from https://advanced.onlinelibrary.wiley.com/doi/10.1002/adma.75433 by Nam-Joon Cho - Shanghai Jiaotong University , Wiley Online Library on [21/10/2026]. See the Terms and Conditions (https://onlinelibrary.wiley.com/terms-and-conditions) on Wiley Online Library for rules of use; OA articles are governed by the applicable Creative Commons License

Consequently, dye removal experiences rapid adsorption at its native pH of 4.3, with a R_e of 93.0%, and exceeds 97.1% at pH 5. Thereafter, subsequent dye adsorption tests were performed with 0.2 g of PDCBs at a native pH of 4.3 for 10 min. Additionally, SEM-EDX elemental analysis of the PDCB's pores after adsorption revealed the additional presence of carbon signals aside from the characteristic silicon and oxygen signals of the PDCBs, providing further evidence of the successful adsorption of organic dyes (Figure 5n).

Nickel ion (Ni^{2+}) is used to represent a typical heavy metal for the adsorption tests. The residual Ni^{2+} concentration after adsorption was quantitatively determined using inductively coupled plasma optical emission spectrometry. The q_t and R_e profiles against mass followed trends similar to those observed for dye adsorption, albeit with a more gradual increase (Figure 5f). Increasing the PDCB mass at a fixed contact time of 2 h produced a gradual, near-linear improvement in Ni^{2+} removal up to 0.4 g, at which removal transitioned gradually into a saturation plateau with a R_e of 81.6%. Further increment in PDCB mass facilitated the complete removal of Ni^{2+} ions at 0.8 g. Therefore, 0.4 g of PDCBs was selected for subsequent experiments, providing a high R_e while retaining sufficient sensitivity to elucidate the influence of the other adsorption parameters. PDCBs exhibited an adsorption profile broadly consistent with that observed for dye removal. PDCBs displayed rapid Ni^{2+} adsorption, reaching 57.8% removal within 10 min, followed by a slower approach to saturation with near-complete removal after 24 h (Figure 5i) [76]. Although R_e exceeded 96% removal after 12 h, 4 h was selected for subsequent experiments as it provided 88.1% removal and a q_t of 2.01 mg g^{-1}, with substantially longer exposure time producing only marginal improvements. Ni^{2+} removal demonstrated strong pH-dependence, with R_e limited to only 15.9% at pH 1 (Figure 5l), whereas further increases in pH resulted in near-complete removal of Ni^{2+} above pH 9. This trend remains consistent with the deprotonation of surface silanol groups, which increases the negatively charged density of PDCBs with increasing pH, strengthening the electrostatic interactions with Ni^{2+}. Although alkaline conditions favored Ni^{2+} removal, subsequent experiments were performed at the native pH of approximately 7, where PDCBs achieved a R_e of 88.1%. This enabled the evaluation of other PDCB types under a fixed, near-neutral condition without interference from a pH-adjusted environment. Additionally, SEM-EDX analysis further confirmed the incorporation of Ni^{2+} after adsorption (Figure 5o). The broader applicability of PDCBs was subsequently evaluated by using copper (Cu^{2+}) as a second heavy metal model. PDCBs demonstrated higher affinity toward Cu^{2+} than Ni^{2+}, achieving near-complete Cu^{2+} removal with a q_t of 2.63 mg g^{-1}, as compared to that of Ni^{2+} (Figure S11). This selectivity persisted in a binary solution containing 100 mg L^{-1} each of Cu^{2+} and Ni^{2+}, with Cu^{2+} removal achieving 94.9% with a q_t of 2.63 mg g^{-1}, whereas Ni^{2+} removal was reported at only 29.4% with a q_t of 0.69 mg g^{-1}. The preferential removal of Cu^{2+} over Ni^{2+} indicates competitive selectivity of PDCBs toward Cu^{2+}. This behavior may be associated with differences in the physicochemical properties of the two ions, including electronegativity, ionic radii, and hydrated radii size, among others. Although similar competitive Cu/Ni removal has been investigated in multi-component systems, with Cu^{2+} reported to demonstrate a higher selectivity as compared to Ni^{2+}, the magnitude and origin of the heavy metal selectivity are strongly dependent on the adsorbent's surface chemistry and solution conditions [77–79].

Amidine latex beads (NPs) were used as a model nanoplastic. The 100 mg L^{-1} NPs solution exhibited an average particle size of 100.75 ± 0.65 nm and a zeta potential of +49.73 mV at its native pH of approximately 7 (Figure S12a,c). Increasing the PDCB mass enhanced the NPs removal, consistent with the greater availability of adsorption sites (Figure 5g). R_e values exceeding 96.3% were obtained at PDCB masses above 0.2 g; therefore, 0.2 g was selected for subsequent experiments. NPs removal experiences a rapid uptake between 1 and 4 h, followed by a slower approach toward near-complete removal at 24 h (Figure 5j). Subsequently, an exposure time of 4 h was adopted as it achieved high removal of 96.3% while avoiding the marginal gains associated with prolonged exposure. The influence of pH on NP removal is presented in Figure 5m. NPs removal was negligible at pH 1, with a R_e of only 0.99%, but increased with increasing pH, exceeding 91.1% R_e at pH > 5. This trend can be attributed to the changes in the surface charge of silica with pH. At pH 1, which is below the silica's isoelectric point (pH ≈ 2–3) [67–70], the silica surface is predominantly positively charged. As the pH increases beyond the isoelectric point, the silanol groups will progressively deprotonate, increasing the negative surface charge density. This promotes stronger electrostatic attraction between the negatively charged PDCB's surface and the positively charged NPs. Since high R_e was achieved at the native suspension pH of approximately 7, subsequent experiments were performed without pH adjustment. Additionally, the zeta potential profile of the NPs demonstrates an increase with pH, up to pH 7 before decreasing at higher pH, with an isoelectric point between pH 11 and 13 (Figure S12a). The initial increase in NPs' zeta potential corresponds with the enhanced removal observed from acidic to near-neutral conditions, elucidating the role of electrostatic attraction between the negatively charged PDCBs and the positively charged NPs. However, NPs removal remained high at alkaline pH despite the declining zeta potential. This discrepancy suggests that continued deprotonation of PDCB surface silanol groups under alkaline conditions increases the negative surface charge density and thereby promotes the removal of positively charged NPs. Moreover, the sustained high R_e at elevated pH may be further attributed to NPs aggregation and the retention of larger aggregates within the PDCB structure. The average particle size increased substantially from 102.77 ± 0.41 nm at pH 11 to 2772 ± 675.80 nm at pH 13, indicating pronounced aggregation. Collectively, both pH-dependent deprotonation of PDCB silanol groups and pH-induced changes in the NPs' colloidal stability contributed to the removal of NPs under alkaline conditions. Additionally, SEM images further revealed nanosphere-like particles retained within the pores of PDCBs, corroborating successful nanoplastic capture (Figure 5p). To further assess the role of electrostatic attraction, negatively charged poly(methyl methacrylate) (PMMA) nanoplastics were used as a control. The PMMA suspension possesses an average particle size of 132.63 ± 0.26 nm, a zeta potential of −50.86 mV, and a native pH of 7.7 (Figure S12b,c). Under otherwise identical conditions, PMMA NPs exhibit minimal uptake by PDCBs, achieving a R_e of only 2.4% and a q_t of 0.11 mg g^{-1}, as compared to the R_e of 96.3% and q_t of 2.23 mg g^{-1} for the NPs (Figure S12d). The pronounced contrast underscores the influence of electrostatic attraction as a dominant mechanism for the removal of cationic pollutants,

15214095, 0, Downloaded from https://advanced.onlinelibrary.wiley.com/doi/10.1002/adma.75433 by Nam-Joon Cho - Shanghai Jiaotong University , Wiley Online Library on [21/10/2026]. See the Terms and Conditions (https://onlinelibrary.wiley.com/terms-and-conditions) on Wiley Online Library for rules of use; OA articles are governed by the applicable Creative Commons License

with a negatively charged surface favoring adsorption of positively charged NPs, whereas electrostatic repulsion restricted the uptake of negatively charged PMMA NPs.

A comparative evaluation of the varying pollen-induced PDCBs (control, lycopodium, sunflower, camellia, olive, and pine) reveals differences in pollutant selectivity (Figure 5q). To clearly observe the impact of these variants, we avoid using the full dose of adsorbents with extremely long exposure time; instead, 0.2, 0.4, and 0.2 g PDCB and 10 min, 4 h, and 4 h exposure time are used for adsorption of dye, Ni^{2+} ions, and NPs, respectively. Interestingly, the pollutant-removal performance does not exhibit a simple monotonic relationship with the overall porosity of the PDCBs. Dye removal remained high across all samples, even for the control variant without pollen, with the recorded R_e above 87.2% for all pollen species and the control achieving a R_e of 75.2%, indicating that dye adsorption is relatively insensitive to the differences in pollen-derived pore architecture within this removal regime. In contrast, pronounced template-dependent differences are observed for Ni^{2+} ions and NPs. Ni^{2+} ions demonstrate obvious selectivity among the PDCB variants with R_e of 48.1%, 88.1%, 68.4%, 63.1%, 60.4%, and 94.1%, respectively for the control, lycopodium, sunflower, camellia, olive, and pine-templated PDCBs. Similarly, NPs' selectivity is distinct, with respective pollen species exhibiting R_e of 25.6%, 96.3%, 62.6%, 98.6%, 99.4%, and 93.2%. Lycopodium- and pine-templated PDCBs exhibit substantially higher Ni^{2+}-ion removal efficiencies, with pine-templated PDCBs exhibiting the highest NP removal. Different pollen morphologies generate distinct pore sizes, shapes, surface topographies, and interconnected porous networks, which, together with porosity and accessible surface area, can regulate liquid penetration, solid–liquid interfacial contact, pollutant accessibility, and mass transport within the beads [80–82]. For nanoscale particulate pollutants, pore geometry and connectivity may additionally influence physical interception, confinement, and retention. Therefore, the observed adsorption behavior arises from the interplay between the pollen-templated pore microenvironment and the size and physicochemical characteristics of the pollutants.

The adsorption performance of PDCBs was further compared with previously reported conventional and advanced adsorbents (Figure 5r and Table S2) [83–96]. The obtained adsorption capacities are comparable to those reported for a range of adsorbents toward dye molecules, Ni^{2+} ions, and NPs. However, because the experimental conditions vary substantially among different studies, including adsorbent dosage, contact time, pH, pollutant concentration, and adsorption method, the comparison is provided as a general reference rather than a direct ranking of adsorption performance. PDCBs outperform most of the existing materials, ranging from bulk adsorbents to engineered particle adsorbents. Notably, PDCBs' adsorption performances were achieved without the need for additional modifications, such as chemical doping, functionalization, or encapsulation to form bulk adsorbents, thereby simplifying the fabrication and recovery process. Moreover, the ideal geometry of PDCBs allows for efficient packing and facile recovery, highlighting their potential for environmental remediation applications due to their multifunctional, practical, and scalable properties.

3 | Conclusion

In summary, this work presents a novel approach for fabricating advanced porous ceramic adsorbents from LMs. Pollen microparticles are strategically employed as hydrophobic particles for the encapsulation of LMs, as components in the synthesis of SPC to promote LM fabrication and as porogens to generate a porous internal structure. Mechanical vibration and UV irradiation trigger the transition of wetting states from CB to CI, enabling deeper infiltration of liquid between surface protrusions and thereby increasing the liquid–solid interfacial contact and the depth of pollen engraving on the PDCB surface. The multilayer configuration of LPB, SPC, and substrate in the collection dish improves the yield, reduces coalescence and guarantees the uniformity of LM production. Furthermore, through the optimized design of fabrication conditions including substrate type, shaking speed, nozzle size, constituent content, the engineered LMGBs are produced at a high yield with uniform size distribution and good sphericity. The pollen and polymer binder are decomposed gradually based on an optimized sintering profile, generating a hierarchical porous architecture featuring pollen-engraved morphologies and micro-interconnected pores distributed across the interior and exterior of PDCBs. The induced porosity elevated the adsorption performance for the removal of Ni^{2+} and NPs, with R_e increased by up to 0.96 and 2.88 times, respectively.

Additionally, the distinct adsorption performances of PDCBs templated by different pollen species reveal a clear structure–performance correlation between the pollen-derived pore architecture and pollutant removal behavior. The combined variations in pore morphology, porosity, accessible surface area, and pore connectivity are expected to regulate pollutant accessibility and transport within the porous network. Lycopodium- and pine-templated PDCBs demonstrated superior removal of Ni^{2+} relative to the other PDCBs. In contrast, all pollen-templated PDCBs achieved consistently high dye removal exceeding 87.2%. NPs removal was also elevated across the samples, exceeding 93.2% for most PDCBs. However, the sunflower-templated PDCB exhibits comparatively lower performance. These differences further suggest the selective role of pollen-templated pore architectures in governing pollutant uptake, likely influenced by diffusion pathways and interactions between the pollutant categories and the porous network.

Furthermore, PDCBs enable easy storage, transportation, packing, and removal within column systems. A proof-of-concept parallelized multi-nozzle fabrication system further demonstrates the scalability of LMGB production and provides a modular route toward higher-throughput PDCB fabrication (Figure S13), which highlights the potential of this strategy for widespread adoption in industrial scale applications. Future studies should evaluate the effects of the solution's ionic strength, competing ions, and dissolved organic matter to assess the robustness and practical applicability of PDCBs in realistic wastewater systems. This study underscores the promising potential of employing biowaste in engineering advanced functional ceramic materials for environmental remediation aligning with the concepts of cross-economy [43], converting waste into high value products through innovative technology or sustainable processing technologies.

15214095, 0, Downloaded from https://advanced.onlinelibrary.wiley.com/doi/10.1002/adma.75433 by Nam-Joon Cho - Shanghai Jiaotong University , Wiley Online Library on [21/10/2026]. See the Terms and Conditions (https://onlinelibrary.wiley.com/terms-and-conditions) on Wiley Online Library for rules of use; OA articles are governed by the applicable Creative Commons License

4 | Experimental Section

4.1 | Materials and Reagents

Defatted pollen powder (pine and olive) was sourced from Greer Laboratories, Inc. Natural raw bee pollen (sunflower and camellia) grains were obtained from Yuensun Biological Technology Co. Ltd. Defatted lycopodium spores, hydrochloric acid (37%, ACS reagent), LUDOX colloidal silica (30, 40, and 50 wt.% suspension in water, 30 nm diameter), copper(II) chloride dihydrate (reagent grade), nickel(II) chloride (98%), perfluorooctyltrichlorosilane (FTS, 97%), poly(ethylene glycol) diacrylate (PEGDA, M_n = 700 g/mol), and 2-hydroxy-2-methylpropiophenone (PI, Darocur 1173; ≥ 96.5%) were all purchased from Sigma-Aldrich. Acetone (AR grade) and amidine latex beads (4 w/v%, 0.1 μm) were bought from Thermo Fisher Scientific. Poly(methyl methacrylate) microspheres (PMMA, 25 mg/mL, 0.1 μm) were bought from Shanghai Yiyuan Biotechnology Co., Ltd. Diethyl ether (AR grade) was sourced from RCI Labscan. *n*-Hexane was obtained from the Tedia Company. Royal Blue 4001 dye was sourced from Pelikan. Potassium hydroxide was obtained from VWR Chemicals. Sodium hydroxide (AR grade) was procured from Schedelco Pte Ltd. SYLGARD 184 silicone elastomer kit (Dow Corning) was used to prepare the PDMS, with a mixing weight ratio of prepolymer and curing agent 10:1. All chemicals were used as received unless stated otherwise. Nylon mesh was sourced from Elko Filtering Co. LLC. Deionized water was obtained using a Milli-Q M water purification system (Merck).

4.2 | Defatting of Natural Raw Bee Pollen Grains

Natural raw bee pollen (sunflower/camellia) grains (500 g) were mixed with 1 L of deionized water and stirred with a disperser (Eurostar 20 digital, IKA) at 1000 rpm at 50°C for 2 h. To remove contaminants, the mixture was filtered through a 200 μm nylon mesh. Pollen paste was formed after removing excess water through vacuum filtration, then it was redispersed in 1 L of acetone and stirred at 1000 rpm at room temperature for 3 h. Excess acetone was removed by vacuum filtration, and the pollen powder was continuously washed with acetone until the filtrate turned clear. The pollen powder was dried in the fume hood for 12 h before mixing with 1 L of diethyl ether and stirring at 1000 rpm at room temperature for 2 h. The process was repeated twice before mixing in fresh diethyl ether and stirring for 12 h. The excess diethyl ether was removed through vacuum filtration and the defatted pollen powder was dried overnight in the fume hood.

4.3 | SPC Fabrication

The SPC was fabricated based on previous work in our group [37]. A PDMS-FTS mixture was obtained by mixing the PDMS and FTS at a mass ratio of 8:2, 0.3 g defatted sunflower pollen was added into the PDMS-FTS mixture at 80 wt.%. Subsequently, *n*-hexane (2 mL) was added and agitated under vortex mixing (Vortex Genie 2) for > 5 min before evenly distributing the mixture on glass slides (75 × 25 mm^2) and drying in the fume hood until *n*-hexane was fully evaporated. Subsequently, the dried coating was left at room temperature for > 7 days to completely cure.

4.4 | LM and LMGB Fabrication

The silica precursors were prepared by mixing 67–72 wt.% LUDOX colloidal silica, 25 wt.% PEGDA, 3 wt.% PI, and 0–5 wt.% of defatted pollen powder. LM were extruded out of a Teflon nozzle using a peristaltic pump (Ismatec, ISM596D, USA) at a fixed rate of 0.35 mL/min and dropped into a collection dish (35 mm × 10 mm, Corning) 30 mm away from the nozzle onto the LPB. The collection dish was coated with SPC and filled to a controlled thickness of LPB (0–4.05 mm). The thickness was controlled by adding different masses of lycopodium pollen (Figure S14). Subsequently, an orbital shaker (Unimax 1010, Heidolph) was utilized to shake the collection dish to induce rolling of the LM promoting sphericity. Afterward, LM green bodies were photocured by a UV light source (Intensilight C-HGFI, Nikon) at an intensity of 37.8 μW/cm^2 with an error of 3.1 μW/cm^2 measured using a UV light meter (SHSE-PUVB, Hangzhou Sensor Technology Co. Ltd.). To investigate the impact of LPB thickness h, silica precursors with 72 wt.% LUDOX (21.6 wt.% silica content) were extruded at a fixed nozzle diameter d = 0.362 mm and shaken at a shaking speed R = 250 rpm. Similarly, the effects of R and d were explored utilizing identical silica precursors at h = 0.98 mm unless otherwise stated. The effects of varying R were explored at a constant d = 0.362 mm, and the effects of varying d were studied at a constant R = 250 rpm. Subsequently, under identical fabrication parameters, the influence of precursor composition on LMGB production was investigated by varying the silica content at 0 wt.% pollen inclusion. Then, at a fixed silica content of 28.8 wt.%, the lycopodium pollen porogens were added at 0–5 wt.%. Finally, silica precursors were held at 71 wt.% LUDOX with 1 wt.% of varying pollen species of lycopodium, sunflower, camellia, olive, and pine pollen to explore the influence of pollen-embedded pores for pollutant selectivity.

4.5 | PDCBs Fabrication

The optimal sintering profiles were designed with reference to the thermal analysis of PDCB's green body. In temperature ranges where rapid weight loss and notable heat flow fluctuations occur, the lower heating rate and prolonged heat preservation were employed to prevent the formation of defects and cracks. The entire sintering process was conducted in an atmosphere of air. First, the green bodies were heated from room temperature to 600°C at a rate of 0.5°C/min and isothermally held for 1 h for the decomposition of binder polymer and pollen particles. Subsequently, the temperature was raised to 950°C at a rate of 1°C/min and isothermally held for 2 h to densify the PDCBs. Afterward, the furnace was cooled to room temperature before obtaining sintered PDCBs.

4.6 | Imaging and Characterization

The material morphologies in this work were analyzed using a variety of microscopes, including a digital microscope (DSX1000, Olympus), scanning electron microscope (7600F, FE-SEM), upright optical microscope (BX60F5, Olympus), and a stereomicroscope (SMZ1000, Nikon). The FTIR spectra of the lycopodium pollen powder, LMGB, and PDCB were measured

15214095, 0, Downloaded from https://advanced.onlinelibrary.wiley.com/doi/10.1002/adma.75433 by Nam-Joon Cho - Shanghai Jiaotong University , Wiley Online Library on [21/10/2026]. See the Terms and Conditions (https://onlinelibrary.wiley.com/terms-and-conditions) on Wiley Online Library for rules of use; OA articles are governed by the applicable Creative Commons License

using an attenuated total reflection FTIR instrument (Frontier, PerkinElmer). The liquid dripping process was captured using a high-speed camera (V1212, Phantom). Contact angles and the air–water surface tension were measured using an optical contact angle measuring instrument (OCA 15 Pro, DataPhysics). The sphericity of LMGBs is quantified using out-of-roundness, OR = $(D_{max}-D_{min})/D_{ave}$ where D_{max}, D_{min}, and D_{ave} are the largest, smallest (measured from the midway point) and average (measured radially 6 times) diameters, respectively. Thermogravimetric analysis and differential scanning calorimetry analysis of LMGBs were concurrently performed under an air atmosphere in thermal analysis equipment (SDT Q600, TA). The temperature was ramped from room temperature to 1150°C at a heating rate of 15°C/min. The PDCBs were ground into powder and analyzed with x-ray diffraction (D8 Advance, Bruker). The internal pore structure of the PDCBs was visualized by micro-computed tomography (micro-CT; Xradia 620 Versa, Zeiss) with a slice interval of 0.3 μm. The open porosities of the PDCBs were determined using a densimeter (SD-200L, 0.0001 g/cm^3 resolution, Alfa Mirage) based on the Archimedes method, as schematically illustrated in Figure S15. The dry mass (W_{dry}), suspended mass in water (W_{sus}), and saturated mass in air (W_{sat}) of PDCBs were measured respectively, and the porosity was calculated as $P\ (\%) = \frac{W_{sat}-W_{dry}}{W_{sat}-W_{sus}} \times 100\%$. The zeta potential and particle size distribution of NPs and PMMA were measured using a zetasizer instrument (Zetasizer Advanced Ultra Red, Malvern). The specific surface area and N_2 adsorption/desorption isotherms were detected using an automated surface area and pore size analyzer (Autosorb-iQ3, Quantachrome, USA).

4.7 | LM Formation Simulations

COMSOL Multiphysics 5.4 was used to simulate the formation of LMs produced through nozzles of various inner diameters d. A two-phase flow model with the level set method was employed to capture the evolving liquid–air interface during LM formation. A 2D axisymmetric model with appropriate boundary conditions was adopted: the inlet boundary at the nozzle was prescribed with a velocity profile corresponding to the experimental ejection conditions; a pressure outlet boundary condition ($p = 0$ Pa) was applied to the far field and no-slip conditions were enforced on the nozzle walls. The computational mesh size was set to 0.0025 mm resulting in a total of 104 613 mesh elements. The computation time for droplet formation was 0.6 s. Image J was used to calculate the diameter of LMs.

4.8 | Dye Adsorption

Batch adsorption experiments were performed to investigate the effects of adsorbent mass, contact time, and solution pH on adsorption performance. Dye concentrations were determined from absorbance at 600 nm using a microplate spectrophotometer (Spark, Tecan) based on the calibration curve (Figure S16). To evaluate the effect of adsorbent mass, different masses of PDCBs (0.01–1.0 g) were immersed in 10 mL of dye solution (0.03035 wt.%) for 1 h. For kinetic studies, 0.2 g of PDCBs was exposed to 10 mL of dye solution for predetermined time intervals (0–4 h). The pH effect was assessed using 0.2 g of PDCBs in 10 mL of dye solution for 10 min over pH 1–13, adjusted with 0.1–2 M HCl or NaOH and measured using a portable pH meter (SevenGo Duo SG23, Mettler Toledo). The adsorption capacity q_t and removal efficiency R_e were calculated as $q_t = ((C_i-C_f) \times V)/m$ and $R_e = (C_i-C_f)/C_i \times 100\%$ where C_i is the initial pollutant concentration (mg L^{-1}), C_f is the final pollutant concentration (mg L^{-1}), V is the volume of solution (L) and m is the adsorbent mass (g) [97]. To compare pollen-derived pore structures, 0.2 g of PDCBs prepared from different pollen species was immersed in 10 mL of unadjusted dye solution (pH ≈ 4.3) for 10 min.

4.9 | Ni^{2+} Adsorption

Batch adsorption experiments were conducted to investigate the effects of adsorbent mass, contact time, and solution pH on Ni^{2+} adsorption. Ni^{2+} and Cu^{2+} solutions (100 mg L^{-1}) were prepared from nickel(II) chloride and copper(II) chloride dihydrate in deionized water. For the adsorbent-mass study, 0.05–1.0 g of PDCBs was added to 10 mL of Ni^{2+} solution for 2 h. For kinetic studies, 0.4 g of PDCBs was exposed to 10 mL of Ni^{2+} solution for 0–24 h. The pH effect was evaluated using 0.4 g of PDCBs in 10 mL of Ni^{2+} solution over pH 1–13. Residual Ni^{2+} concentrations were quantified by inductively coupled plasma optical emission spectrometry (ICP–OES; Avio 550 Max, PerkinElmer), and the adsorption capacity (q_t) and removal efficiency (R_e) were calculated accordingly. For comparison with another heavy-metal ion, 0.4 g of PDCBs was exposed to 10 mL of Cu^{2+} solution (100 mg L^{-1}, pH ≈ 6.0) for 4 h. Competitive adsorption was further evaluated in a binary solution containing 100 mg L^{-1} each of Ni^{2+} and Cu^{2+} (pH 5.7) for 4 h. To examine the effect of pollen-derived pore structures, 0.4 g of PDCBs prepared from different pollen species was immersed in 10 mL of unadjusted Ni^{2+} solution (100 mg L^{-1}, pH ≈ 7.0) for 4 h.

4.10 | Nanoplastics Adsorption

Batch adsorption experiments were conducted to investigate the effects of adsorbent mass, contact time, and solution pH on nanoplastic adsorption. Amidine latex nanoparticle and PMMA nanoparticle dispersions (100 mg L^{-1}) were prepared in ultrapure deionized water (Millipore Direct-Q 3 UV, Merck), respectively. Both amidine latex and PMMA nanoplastics concentrations were determined from absorbance at 350 nm using a microplate spectrophotometer based on a calibration curve (Figure S17). For the adsorbent-mass study, 0.05–1.0 g of PDCBs was exposed to the nanoparticle dispersion for 4 h. For kinetic studies, 0.2 g of PDCBs was immersed in 5 mL of nanoparticle dispersion for 0–24 h. The pH effect was evaluated using 0.2 g of PDCBs in 5 mL of nanoparticle dispersion over pH 1–13. The adsorption capacity (q_t) and removal efficiency (R_e) were calculated from the residual nanoparticle concentrations. To investigate the role of electrostatic interactions, negatively charged PMMA nanoparticles (100 mg L^{-1}) were tested under otherwise identical conditions using 0.2 g of PDCBs for 4 h. To evaluate the effect of pollen-derived pore structures, 0.2 g of PDCBs prepared from different pollen species were exposed to 5 mL of unadjusted amidine latex nanoparticle dispersion (100 mg L^{-1}, pH ≈ 7.0) for 4 h.

15214095, 0, Downloaded from https://advanced.onlinelibrary.wiley.com/doi/10.1002/adma.75433 by Nam-Joon Cho - Shanghai Jiaotong University , Wiley Online Library on [21/10/2026]. See the Terms and Conditions (https://onlinelibrary.wiley.com/terms-and-conditions) on Wiley Online Library for rules of use; OA articles are governed by the applicable Creative Commons License

Author Contributions

Chenchen Zhou: conceptualization, investigation, writing – original draft, methodology, writing – review and editing, visualization, validation, formal analysis, data curation, supervision, and software. **Jun Hao Mo**: investigation, writing – original draft, methodology, validation, visualization, data curation, formal analysis, and writing – review and editing. **Ruiyan Ni**: investigation, writing – review and editing, validation, formal analysis, and visualization. **Zihao Guo**: investigation, methodology, formal analysis, data curation, and writing – original draft. **Yanzhang Xu**: software, investigation, and writing – original draft. **Xinyue Zhang**: methodology, formal analysis, data curation, and software. **Hanna Kim**: data curation, methodology, formal analysis, and investigation. **Jian Li**: investigation and methodology. **Ibrahim Shahrudin Mohammed**: validation, investigation, and methodology. **Munho Kim**: supervision, writing – review and editing, and formal analysis. **Bernard P. Binks**: supervision, writing – review and editing, and formal analysis. **Nam-Joon Cho**: supervision, project administration, writing – review and editing, validation, conceptualization, funding acquisition, and resources.

Acknowledgements

We thank C. Lai and M. Kong for borrowing the high-speed camera and helping to capture footage for liquid marble formation. We also thank all the TSSM group members for their various supports. This study was supported by the Ministry of Education in Singapore under the MOE AcRF Tier 3 grant (grant no. MOE-MOET32022-0002), Research start-up funding from Shanghai Jiao Tong University (grant no. WL220202009), as well as the Korea Health Technology R&D Project through the Korea Health Industry Development Institute (KHIDI), funded by the Ministry of Health & Welfare, Republic of Korea (grant no. HI22C1394) and Ministry of Agriculture, Food and Rural Affairs (grant no. RS-2024-00403067).

Funding

This study was supported by the Ministry of Education in Singapore under the MOE AcRF Tier 3 grant (grant no. MOE-MOET32022-0002), Research start-up funding from Shanghai Jiao Tong University (grant no. WL220202009), as well as the Korea Health Technology R&D Project through the Korea Health Industry Development Institute (KHIDI), funded by the Ministry of Health & Welfare, Republic of Korea (grant no. HI22C1394) and Ministry of Agriculture, Food and Rural Affairs (grant no. RS-2024-00403067).

Conflicts of Interest

The authors declare no conflicts of interest.

Data Availability Statement

The data that support the findings of this study are available from the corresponding author upon reasonable request.

References

1. J. Saczek, X. Yao, V. Zivkovic, et al., "Long-Lived Liquid Marbles for Green Applications," *Advanced Functional Materials* 31 (2021): 2011198, https://doi.org/10.1002/adfm.202011198.

2. N. M. Oliveira, R. L. Reis, and J. F. Mano, "The Potential of Liquid Marbles for Biomedical Applications: A Critical Review," *Advanced Healthcare Materials* 6 (2017): 1700192, https://doi.org/10.1002/adhm.201700192.

3. E. Bormashenko, "Liquid Marbles: Properties and Applications," *Current Opinion in Colloid & Interface Science* 16 (2011): 266–271, https://doi.org/10.1016/j.cocis.2010.12.002.

4. R. Murakami, N. Kanda, and M. Yamamoto, "Mechanism of Multilayer Formation on Liquid Marbles," *Colloid and Interface Science Communications* 47 (2022): 100607, https://doi.org/10.1016/j.colcom.2022.100607.

5. P. Aussillous and D. Quéré, "Liquid Marbles," *Nature* 411 (2001): 924–927, https://doi.org/10.1038/35082026.

6. L. Forny, I. Pezron, K. Saleh, P. Guigon, and L. Komunjer, "Storing Water in Powder Form by Self-Assembling Hydrophobic Silica Nanoparticles," *Powder Technology* 171 (2007): 15–24, https://doi.org/10.1016/j.powtec.2006.09.006.

7. M. Tenjimbayashi, T. Mouterde, P. K. Roy, and K. Uto, "Liquid Marbles: Review of Recent Progress in Physical Properties, Formation Techniques, and Lab-in-a-Marble Applications in Microreactors and Biosensors," *Nanoscale* 15 (2023): 18980–18998, https://doi.org/10.1039/D3NR04966C.

8. J. Jin, Z. Huang, Y. Xie, Z. Shen, B. Liu, and H. Chen, "Fabrication of Stable Monolayer Liquid Marbles With Reduced Particle Coverage and Locomotion on Hydrophilic Surface," *Communications Materials* 5 (2024): 64, https://doi.org/10.1038/s43246-024-00504-5.

9. Y. Sun, Y. Zheng, C. Liu, et al., "Liquid Marbles, Floating Droplets: Preparations, Properties, Operations and Applications," *RSC Advances* 12 (2022): 15296, https://doi.org/10.1039/d2ra00735e.

10. M. Paven, H. Mayama, T. Sekido, H.-J. Butt, Y. Nakamura, and S. Fujii, "Light-Driven Delivery and Release of Materials Using Liquid Marbles," *Advanced Functional Materials* 26 (2016): 3199–3206, https://doi.org/10.1002/adfm.201600034.

11. Y. Tsumura, K. Oyama, A.-L. Fameau, et al., "Photo/Thermo Dual Stimulus-Responsive Liquid Marbles Stabilized With Polypyrrole-Coated Stearic Acid Particles," *ACS Applied Materials & Interfaces* 14 (2022): 41618–41628, https://doi.org/10.1021/acsami.2c12681.

12. N. Barman, A. Shome, S. Kumar, et al., "Preprogramming Floating Time of Liquid Marble," *Advanced Functional Materials* 33 (2023): 2214840, https://doi.org/10.1002/adfm.202214840.

13. Y. Xue, H. Wang, Y. Zhao, et al., "Magnetic Liquid Marbles: A "Precise" Miniature Reactor," *Advanced Materials* 22 (2010): 4814–4818, https://doi.org/10.1002/adma.201001898.

14. W. Jiang, X. Guan, W. Liu, Y. Li, H. Jiang, and T. Ngai, "Rotating Liquid Marble Microreactors for Enhanced Enzymatic Reactions," *Advanced Functional Materials* 35 (2025): 2504193, https://doi.org/10.1002/adfm.202504193.

15. X. Lin, M. Duan, H. Zhang, et al., "Multiwell Plate Integrated With Transparent Liquid Marbles for 3D Cell Culturing," *Droplet* 4, (2025): 164, https://doi.org/10.1002/dro2.164.

16. M. Liu, C. Chen, J. Yu, et al., "The Gelatin-Based Liquid Marbles for Cell Cryopreservation," *Materials Today Bio* 17 (2022): 100477, https://doi.org/10.1016/j.mtbio.2022.100477.

17. G. McHale and M. I. Newton, "Liquid Marbles: Principles and Applications," *Soft Matter* 7 (2011): 5473, https://doi.org/10.1039/c1sm05066d.

18. G. McHale and M. I. Newton, "Liquid Marbles: Topical Context Within Soft Matter and Recent Progress," *Soft Matter* 11 (2015): 2530–2546, https://doi.org/10.1039/C5SM00084J.

19. Z. Wang, Y. Chu, G. Zhao, et al., "Study of Surface Wettability of Mineral Rock Particles by an Improved Washburn Method," *ACS Omega* 8 (2023): 15721, https://doi.org/10.1021/acsomega.3c01352.

20. A. Peethan, S. D. George, and M. Aravind, *Advances in Superhydrophobic Coatings*, ed. V. S. Saji (Royal Society Of Chemistry, 2023), 1–25, https://doi.org/10.1039/9781837670031-00001.

21. A. Sneha Ravi and S. Dalvi, "Liquid Marbles and Drops on Superhydrophobic Surfaces: Interfacial Aspects and Dynamics of Formation: A Review," *ACS Omega* 9 (2024): 12307, https://doi.org/10.1021/acsomega.3c07657.

22. K. L. Wilke, Z. Lu, Y. Song, and E. N. Wang, "Turning Traditionally Nonwetting Surfaces Wetting for Even Ultra-High Surface Energy Liquids," *PNAS* 119 (2022): 1, https://doi.org/10.1073/pnas.2109052119.

15214095, 0, Downloaded from https://advanced.onlinelibrary.wiley.com/doi/10.1002/adma.75433 by Nam-Joon Cho - Shanghai Jiaotong University , Wiley Online Library on [21/10/2026]. See the Terms and Conditions (https://onlinelibrary.wiley.com/terms-and-conditions) on Wiley Online Library for rules of use; OA articles are governed by the applicable Creative Commons License

23. U. Sultan, C. Kotulla, K. Kefle, S. Fujii, and N. Vogel, "Rough and Tough: How Particle Surface Roughness Affects Liquid Marble Formation and Stability," *Advanced Science* 12 (2025): 2501378, https://doi.org/10.1002/advs.202501378.

24. B. T. Lobel, C. A. Thomas, P. M. Ireland, E. J. Wanless, and G. B. Webber, "Liquid Marbles, Formation and Locomotion Using External Fields and Forces," *Advanced Powder Technology* 32 (2021): 1823–1832, https://doi.org/10.1016/j.apt.2021.04.022.

25. F. Geyer, Y. Asaumi, D. Vollmer, H.-J. Butt, Y. Nakamura, and S. Fujii, "Polyhedral Liquid Marbles," *Advanced Functional Materials* 29 (2019): 1808826, https://doi.org/10.1002/adfm.201808826.

26. M. Tenjimbayashi, S. Samitsu, and M. Naito, "Simultaneous Detection and Repair of Wetting Defects in Superhydrophobic Coatings via Cassie–Wenzel Transitions of Liquid Marbles," *Advanced Functional Materials* 29 (2019): 1900688, https://doi.org/10.1002/adfm.201900688.

27. E. Bormashenko, T. Stein, R. Pogreb, and D. Aurbach, ""Petal Effect" on Surfaces Based on Lycopodium: High-Stick Surfaces Demonstrating High Apparent Contact Angles," *Journal of Physical Chemistry C* 113 (2009): 5568–5572, https://doi.org/10.1021/jp900594k.

28. C. Lv, X. Zhang, F. Niu, F. He, and P. Hao, "From Initial Nucleation to Cassie-Baxter State of Condensed Droplets on Nanotextured Superhydrophobic Surfaces," *Scientific Reports* 7 (2017): 42752, https://doi.org/10.1038/srep42752.

29. E. Bormashenko, R. Pogreb, T. Stein, et al., "Characterization of Rough Surfaces With Vibrated Drops," *Physical Chemistry Chemical Physics* 10 (2008): 4056, https://doi.org/10.1039/b800091c.

30. K. S. Germain, Y.-C. Sun, S. Shu, and H. E. Naguib, "Active Superhydrophobic Surfaces With Switchable Wettability: A Review," *Smart Materials and Structures* 34 (2025): 063001, https://doi.org/10.1088/1361-665X/add3df.

31. S. Fujii, S. Yusa, and Y. Nakamura, "Stimuli-Responsive Liquid Marbles: Controlling Structure, Shape, Stability, and Motion," *Advanced Functional Materials* 26 (2016): 7206–7223, https://doi.org/10.1002/adfm.201603223.

32. E.-L. Tan, M. G. Potroz, G. Ferracci, et al., "Light-Induced Surface Modification of Natural Plant Microparticles: Toward Colloidal Science and Cellular Adhesion Applications," *Advanced Functional Materials* 28 (2018): 1707568, https://doi.org/10.1002/adfm.201707568.

33. S. Zhou, D. Wu, Z. Xu, and Q. Jiang, "Sporopollenin Exine Capsules With Polypeptide Multilayer Films Promoting Cell Adhesion," *Chemical Engineering Journal* 475 (2023): 145607, https://doi.org/10.1016/j.cej.2023.145607.

34. T.-F. Fan, S. Park, Q. Shi, et al., "Transformation of Hard Pollen Into Soft Matter," *Nature Communications* 11 (2020): 1449, https://doi.org/10.1038/s41467-020-15294-w.

35. C. Zhou, J. Deng, J. H. Tay, et al., "Multifunctional Material Building Blocks From Plant Pollen," *Annual Review of Chemical and Biomolecular Engineering* 15 (2024): 1–24, https://doi.org/10.1146/annurev-chembioeng-101121-085959.

36. E. Alpizar-Reyes, J. L. Concha, F. J. Martín-Martínez, and J. Norambuena-Contreras, "Biobased Spore Microcapsules for Asphalt Self-Healing," *ACS Applied Materials & Interfaces* 14 (2022): 31296–31311, https://doi.org/10.1021/acsami.2c07301.

37. J. Li, J. Deng, C. Zhou, et al., "Biomimetic Superhydrophobic Surfaces by Nanoarchitectonics With Natural Sunflower Pollen," *Small* 21 (2025): 2409136, https://doi.org/10.1002/smll.202409136.

38. T. Chen, D. Wang, Q. Cao, H. Xiong, X. Chen, and Y. Fan, "Optimizing Photocuring Properties of Ceramic Slurry for 3D Printing of Ceramic Membranes," *Ceramics International* 50 (2024): 1732–1741, https://doi.org/10.1016/j.ceramint.2023.10.272.

39. W.-Y. Maeng, J.-B. Lee, Y.-H. Koh, and H.-E. Kim, "Innovative in Situ Photocuring-Assisted 3D Plotting Technique for Complex-Shaped Ceramic Architectures With High Shape Retention," *Ceramics International* 45 (2019): 8440–8447, https://doi.org/10.1016/j.ceramint.2019.01.153.

40. T. Ohji and M. Fukushima, "Macro-Porous Ceramics: Processing and Properties," *International Materials Reviews* 57 (2012): 115–131, https://doi.org/10.1179/1743280411Y.0000000006.

41. Y. Chen, N. Wang, O. Ola, Y. Xia, and Y. Zhu, "Porous Ceramics: Light in Weight but Heavy in Energy and Environment Technologies," *Materials Science and Engineering: R: Reports* 143 (2021): 100589, https://doi.org/10.1016/j.mser.2020.100589.

42. M. S. Ibrahim, A. R. Ferhan, C. Zhou, et al., "Allergen to Asset: Pollen-Based Drug Delivery Systems," *Advanced Drug Delivery Reviews* 224 (2025): 115643, https://doi.org/10.1016/j.addr.2025.115643.

43. N.-J. Cho, "Preparing for Tomorrow With Materials Today," *Materials Today* 61 (2022): 1–3, https://doi.org/10.1016/j.mattod.2022.11.006.

44. F.-S. Li, P. Phyo, J. Jacobowitz, M. Hong, and J.-K. Weng, "The Molecular Structure of Plant Sporopollenin," *Nature Plants* 5 (2019): 41–46, https://doi.org/10.1038/s41477-018-0330-7.

45. P. Atkins, J. de Paula, and J. Keeler, *Physical Chemistry* (Oxford University Press, 2022).

46. E. Bormashenko and R. Grynyov, "Plasma Treatment Allows Water Suspending of the Natural Hydrophobic Powder (lycopodium)," *Colloids and Surfaces B: Biointerfaces* 97 (2012): 171–174, https://doi.org/10.1016/j.colsurfb.2012.04.015.

47. E. Bormashenko, "Wetting Transitions on Biomimetic Surfaces," *Philosophical Transactions: Mathematical, Physical and Engineering Sciences* 368 (2010): 4695, https://doi.org/10.1098/rsta.2010.0121.

48. B. P. Binks and T. S. Horozov, *Colloidal Particles at Liquid Interfaces* (Cambridge University Press, 2006), https://doi.org/10.1017/CBO9780511536670.

49. A. Mozhi Devan Padmanathan, A. Sneha Ravi, H. Choudhary, S. N. Varanakkottu, and S. V. Dalvi, "Predictive Framework for the Spreading of Liquid Drops and the Formation of Liquid Marbles on Hydrophobic Particle Bed," *Langmuir* 35 (2019): 6657, https://doi.org/10.1021/acs.langmuir.9b00698.

50. C. S. Bailey, J. S. Zarins-Tutt, M. Agbo, et al., "A Natural Solution to Photoprotection and Isolation of the Potent Polyene Antibiotic, Marinomycin A," *Chemical Science* 10 (2019): 7549–7553, https://doi.org/10.1039/C9SC01375J.

51. C. Zhou, S. Liang, Y. Li, H. Chen, and J. Li, "Fabrication of Sharp-Edged 3D Microparticles via Folded PDMS Microfluidic Channels," *Lab on a Chip* 22 (2022): 148–155, https://doi.org/10.1039/D1LC00807B.

52. C. Zhou, Y. Cao, C. Liu, and W. Guo, "Microparticles by Microfluidic Lithography," *Materials Today* 67 (2023): 178, https://doi.org/10.1016/j.mattod.2023.05.009.

53. Y. Zeng and R. von Klitzing, "Structuring of Colloidal Suspensions Confined between a Silica Microsphere and an Air Bubble," *Soft Matter* 7 (2011): 5329, https://doi.org/10.1039/c0sm01487g.

54. S. Cerveny, G. A. Schwartz, J. Otegui, J. Colmenero, J. Loichen, and S. Westermann, "Dielectric Study of Hydration Water in Silica Nanoparticles," *Journal of Physical Chemistry C* 116 (2012): 24340–24349, https://doi.org/10.1021/jp307826s.

55. A. M. Schrader, J. I. Monroe, R. Sheil, et al., "Surface Chemical Heterogeneity Modulates Silica Surface Hydration," *Proceedings of the National Academy of Sciences* 115 (2018): 2890–2895, https://doi.org/10.1073/pnas.1722263115.

56. B. McLean and I. Yarovsky, "Structure, Properties, and Applications of Silica Nanoparticles: Recent Theoretical Modeling Advances, Challenges, and Future Directions," *Small* 20 (2024): 2405299, https://doi.org/10.1002/smll.202405299.

57. Z. Cheng, H. Shan, Y. Sun, L. Zhang, H. Jiang, and C. Li, "Evolution Mechanism of Surface Hydroxyl Groups of Silica During Heat Treat-

15214095, 0, Downloaded from https://advanced.onlinelibrary.wiley.com/doi/10.1002/adma.75433 by Nam-Joon Cho - Shanghai Jiaotong University , Wiley Online Library on [21/10/2026]. See the Terms and Conditions (https://onlinelibrary.wiley.com/terms-and-conditions) on Wiley Online Library for rules of use; OA articles are governed by the applicable Creative Commons License

ment," *Applied Surface Science* 513 (2020): 145766, https://doi.org/10.1016/j.apsusc.2020.145766.

58. T. W. Dijkstra, R. Duchateau, R. A. Van Santen, A. Meetsma, and G. P. A. Yap, "Silsesquioxane Models for Geminal Silica Surface Silanol Sites. A Spectroscopic Investigation of Different Types of Silanols," *Journal of the American Chemical Society* 124 (2002): 9856–9864, https://doi.org/10.1021/ja0122243.

59. R. Xie, A. R. Weisen, Y. Lee, et al., "Glass Transition Temperature From the Chemical Structure of Conjugated Polymers," *Nature Communications* 11 (2020): 893, https://doi.org/10.1038/s41467-020-14656-8.

60. C. L. Beyler and M. M. Hirschler, "Thermal Decomposition of Polymers," in *SFPE Handbook of Fire Protection Engineering* (SFPE, 2002), 111–131.

61. H. Guo, P. Yuan, B. Zhang, Q. Wang, L. Deng, and D. Liu, "Realization of High-Percentage Addition of Fly Ash in the Materials for the Preparation of Geopolymer Derived From Acid-Activated Metakaolin," *Journal of Cleaner Production* 285 (2021): 125430, https://doi.org/10.1016/j.jclepro.2020.125430.

62. S. Ronka, "Properties of Novel Spherical Carbon Adsorbents Synthesized From Phosphorylated Polymeric Precursors," *Journal of Analytical and Applied Pyrolysis* 110 (2014): 390–400, https://doi.org/10.1016/j.jaap.2014.10.012.

63. Z. Liu, L. Qu, X. Li, X. Jiang, and L. Yu, "Design of Carbon Materials With Controllable Morphology for Efficient Adsorption of Cu(II) Ion and Electromagnetic Wave Absorption," *Separation and Purification Technology* 356 (2025): 130008, https://doi.org/10.1016/j.seppur.2024.130008.

64. C.-H. Liu, H.-T. Jiang, and C.-H. Wang, "Fabrication and Characterization of a Toughened Spherical Chitosan Adsorbent Only through Physical Crosslinking Based on Mechanism of Chain Rearrangement," *RSC Advances* 12 (2022): 9179, https://doi.org/10.1039/d1ra09438f.

65. S. Shabani, S. Mohammad Mirkazemi, B. Mohammadi, M. Magni, and S. Trasatti, "Spherical Gamma-Alumina Macroscopic Beads as Easy to Remove Adsorbents for Water Remediation: Modeling of Indigo Carmine Case Study," *Applied Surface Science* 676 (2024): 161019, https://doi.org/10.1016/j.apsusc.2024.161019.

66. A. Ben Amor, M. Arenas, J. Martín, et al., "Alginate/Geopolymer Hybrid Beads as an Innovative Adsorbent Applied to the Removal of 5-Fluorouracil From Contaminated Environmental Water," *Chemosphere* 335 (2023): 139092, https://doi.org/10.1016/j.chemosphere.2023.139092.

67. T. Jesionowski, "Synthesis of Organic–inorganic Hybrids via Adsorption of Dye on an Aminosilane-Functionalised Silica Surface," *Dyes and Pigments* 55 (2002): 133–141, https://doi.org/10.1016/S0143-7208(02)00105-5.

68. M. L. Hair, "Hydroxyl Groups on Silica Surface," *Journal of Non-Crystalline Solids* 19 (1975): 299–309, https://doi.org/10.1016/0022-3093(75)90095-2.

69. J. Yang and E. G. Wang, "Reaction of Water on Silica Surfaces," *Current Opinion in Solid State and Materials Science* 10 (2006): 33–39, https://doi.org/10.1016/j.cossms.2006.02.001.

70. L. Dalstein, E. Potapova, and E. Tyrode, "The Elusive Silica/Water Interface: Isolated Silanols Under Water as Revealed by Vibrational Sum Frequency Spectroscopy," *Physical Chemistry Chemical Physics* 19 (2017): 10343–10349, https://doi.org/10.1039/C7CP01507K.

71. S. Zeb, N. Ali, Z. Ali, et al., "Silica-Based Nanomaterials as Designer Adsorbents to Mitigate Emerging Organic Contaminants From Water Matrices," *Journal of Water Process Engineering* 38 (2020): 101675, https://doi.org/10.1016/j.jwpe.2020.101675.

72. S. K. Parida, S. Dash, S. Patel, and B. K. Mishra, "Adsorption of Organic Molecules on Silica Surface," *Advances in Colloid and Interface Science* 121 (2006): 77–110, https://doi.org/10.1016/j.cis.2006.05.028.

73. A. M. Saleh, H. H. Mahdi, A. B. Alias, et al., "Equilibrium and Kinetic Studies in Adsorption of H2S Using Coconut Shell Activated Carbon Xerogel: Effect of Mass Adsorbent and Temperature," *Desalination and Water Treatment* 317 (2024): 100149, https://doi.org/10.1016/j.dwt.2024.100149.

74. A. Hashem, C. O. Aniagor, S. Farag, M. Fikry, A. A. Aly, and A. Amr, "Evaluation of the Adsorption Capacity of Surfactant-Modified Biomass in an Aqueous Acid Blue 193 System," *Waste Management Bulletin* 2 (2024): 172–183, https://doi.org/10.1016/j.wmb.2024.01.004.

75. C. O. Aniagor, M. A. Afifi, and A. Hashem, "Modelling of Basic Blue-9 Dye Sorption Onto Hydrolyzed Polyacrylonitrile Grafted Starch Composite," *Carbohydrate Polymer Technologies and Applications* 2 (2021): 100141, https://doi.org/10.1016/j.carpta.2021.100141.

76. R. Beksissa, B. Tekola, T. Ayala, and B. Dame, "Investigation of the Adsorption Performance of Acid Treated Lignite Coal for Cr (VI) Removal From Aqueous Solution," *Environmental Challenges* 4 (2021): 100091, https://doi.org/10.1016/j.envc.2021.100091.

77. J. Kang, H. Li, A. Wang, et al., "Competitive Adsorption and Removal Mechanisms of Cu2+ and Ni2+ by Hydrophobic Soluble Microbial Products in Activated Sludge," *Chemical Engineering Science* 330 (2026): 123855, https://doi.org/10.1016/j.ces.2026.123855.

78. D. Humelnicu, M. M. Lazar, M. Ignat, I. A. Dinu, E. S. Dragan, and M. V. Dinu, "Removal of Heavy Metal Ions From Multi-Component Aqueous Solutions by Eco-Friendly and Low-Cost Composite Sorbents With Anisotropic Pores," *Journal of Hazardous Materials* 381 (2020): 120980, https://doi.org/10.1016/j.jhazmat.2019.120980.

79. Z. Mahdi, Q. J. Yu, and A. El Hanandeh, "Investigation of the Kinetics and Mechanisms of Nickel and Copper Ions Adsorption From Aqueous Solutions by Date Seed Derived Biochar," *Journal of Environmental Chemical Engineering* 6 (2018): 1171–1181, https://doi.org/10.1016/j.jece.2018.01.021.

80. Z. Zhao, C. Ling, D. Wang, et al., "Liquid Marbles in Liquid," *Small* 16 (2020): 2002802, https://doi.org/10.1002/smll.202002802.

81. R. Xiao, G. Yu, B. B. Xu, N. Wang, and X. Liu, "Fiber Surface/Interfacial Engineering on Wearable Electronics," *Small* 17 (2021): 2102903, https://doi.org/10.1002/smll.202102903.

82. D. Wang, Y. Liu, S. Sridhar, et al., "Biaxially Morphing Droplet Shape by an Active Surface," *Advanced Materials Interfaces* 8 (2021): 2001199, https://doi.org/10.1002/admi.202001199.

83. H. Karaca, E. Altıntığ, D. Türker, and M. Teker, "An Evaluation of Coal Fly Ash as an Adsorbent for the Removal of Methylene Blue From Aqueous Solutions: Kinetic and Thermodynamic Studies," *Journal of Dispersion Science and Technology* 39 (2018): 1800–1807, https://doi.org/10.1080/01932691.2018.1462191.

84. S. Yadav, A. Asthana, R. Chakraborty, et al., "Cationic Dye Removal Using Novel Magnetic/Activated Charcoal/β-Cyclodextrin/Alginate Polymer Nanocomposite," *Nanomaterials* 10 (2020): 170, https://doi.org/10.3390/nano10010170.

85. D. Morales-Urrea and A. López-Córdoba, "Mechanistic Modeling of pH-Dependent Adsorption of Methylene Blue on Thermally Stabilized Electrospun Polyvinyl Alcohol Membranes Containing Clinoptilolite," *Journal of Polymers and the Environment* 34 (2026): 166, https://doi.org/10.1007/s10924-026-03864-w.

86. J. Fito, S. Abrham, and K. Angassa, "Adsorption of Methylene Blue From Textile Industrial Wastewater Onto Activated Carbon of Parthenium Hysterophorus," *International Journal of Environmental Research* 14 (2020): 501–511, https://doi.org/10.1007/s41742-020-00273-2.

87. J. Zhou, M. Li, Y. Tao, and L. Zha, "Study on the Adsorption Characteristics of Methylene Blue by Magnesium-Modified Fly Ash," *Molecules* 30 (2025): 992, https://doi.org/10.3390/molecules30050992.

88. M. E. Argun, S. Dursun, K. Gur, C. Ozdemir, M. Karatas, and S. Dogan, "Nickel Adsorption on the Modified Pine Tree Materials," *Environmental Technology* 26 (2005): 479–488, https://doi.org/10.1080/09593332608618532.

15214095, 0, Downloaded from https://advanced.onlinelibrary.wiley.com/doi/10.1002/adma.75433 by Nam-Joon Cho - Shanghai Jiaotong University , Wiley Online Library on [21/10/2026]. See the Terms and Conditions (https://onlinelibrary.wiley.com/terms-and-conditions) on Wiley Online Library for rules of use; OA articles are governed by the applicable Creative Commons License

89. V. K. Gupta, C. K. Jain, I. Ali, M. Sharma, and V. K. Saini, "Removal of Cadmium and Nickel From Wastewater Using Bagasse Fly Ash—A Sugar Industry Waste," *Water Research* 37 (2003): 4038–4044, https://doi.org/10.1016/S0043-1354(03)00292-6.

90. M. Mohammadi, A. Ghaemi, M. Torab-Mostaedi, M. Asadollahzadeh, and A. Hemmati, "Adsorption of Cadmium (II) and Nickel (II) on Dolomite Powder," *Desalination and Water Treatment* 53 (2015): 149–157, https://doi.org/10.1080/19443994.2013.836990.

91. M. G. A. Vieira, A. F. A. Neto, M. L. Gimenes, and M. G. C. da Silva, "Sorption Kinetics and Equilibrium for the Removal of Nickel Ions From Aqueous Phase on Calcined Bofe Bentonite Clay," *Journal of Hazardous Materials* 177 (2010): 362–371, https://doi.org/10.1016/j.jhazmat.2009.12.040.

92. J. Goel, K. Kadirvelu, C. Rajagopal, and V. K. Garg, "Investigation of Adsorption of Lead, Mercury and Nickel From Aqueous Solutions Onto Carbon Aerogel," *Journal of Chemical Technology & Biotechnology* 80 (2005): 469–476, https://doi.org/10.1002/jctb.1212.

93. M. Urso, M. Ussia, F. Novotný, and M. Pumera, "Trapping and Detecting Nanoplastics by MXene-Derived Oxide Microrobots," *Nature Communications* 13 (2022): 3573, https://doi.org/10.1038/s41467-022-31161-2.

94. P. Dong, Y. Liang, C. Shen, E. Jiang, and S. A. Bradford, "Dual Roles of Goethite Coating on the Transport of Plastic Nanoparticles in Heterogeneous Porous Media: The Significance of Collector Surface Roughness," *Journal of Hazardous Materials* 470 (2024): 134153, https://doi.org/10.1016/j.jhazmat.2024.134153.

95. J. Sun, Y. Wang, Y. He, et al., "Effective Removal of Nanoplastics From Water by Cellulose/MgAl Layered Double Hydroxides Composite Beads," *Carbohydrate Polymers* 298 (2022): 120059, https://doi.org/10.1016/j.carbpol.2022.120059.

96. M. Ko, T. Jang, S. Yoon, et al., "Synthesis of Recyclable and Light-Weight Graphene Oxide/Chitosan/Genipin Sponges for the Adsorption of Diclofenac, Triclosan, and Microplastics," *Chemosphere* 356 (2024): 141956, https://doi.org/10.1016/j.chemosphere.2024.141956.

97. C. Liu, W. Wang, N. Wang, et al., "Synthesis of Cubic Mesoporous Silica SBA16 Functionalized With Carboxylic Acid in a One-Pot Process for Efficient Removal of Wastewater Containing Cu2+: Adsorption Isotherms, Kinetics, and Thermodynamics," *Microporous and Mesoporous Materials* 382 (2025): 113402, https://doi.org/10.1016/j.micromeso.2024.113402.

Supporting Information

Additional supporting information can be found online in the Supporting Information section.

Supporting File 1: adma75433-sup-0001-SuppMat.docx.
Supporting File 2: adma75433-sup-0002-VideoS1.avi.
Supporting File 3: adma75433-sup-0003-VideoS2.avi.
Supporting File 4: adma75433-sup-0004-VideoS3.avi.
Supporting File 5: adma75433-sup-0005-VideoS4.avi.
Supporting File 6: adma75433-sup-0006-VideoS5.avi.
Supporting File 7: adma75433-sup-0007-VideoS6.avi.
Supporting File 8: adma75433-sup-0008-VideoS7.avi.
Supporting File 9: adma75433-sup-0009-VideoS8.avi.
Supporting File 10: adma75433-sup-0010-VideoS9.mp4.
Supporting File 11: adma75433-sup-0011-VideoS10.avi.
Supporting File 12: adma75433-sup-0012-VideoS11.avi.
Supporting File 13: adma75433-sup-0013-VideoS12.avi.

15214095, 0, Downloaded from https://advanced.onlinelibrary.wiley.com/doi/10.1002/adma.75433 by Nam-Joon Cho - Shanghai Jiaotong University , Wiley Online Library on [21/10/2026]. See the Terms and Conditions (https://onlinelibrary.wiley.com/terms-and-conditions) on Wiley Online Library for rules of use; OA articles are governed by the applicable Creative Commons License